Monthly Notices
of the
ROYAL ASTRONOMICAL SOCIETY

MNRAS **525,** 3879–3895 (2023) https://doi.org/10.1093/mnras/stad2401
Advance Access publication 2023 September 4

Uchuu–ν^2GC galaxies and AGN: cosmic variance forecasts of high-redshift AGN for JWST, *Euclid*, and LSST

Taira Oogi,[1,2★] Tomoaki Ishiyama,[2] Francisco Prada,[3] Manodeep Sinha,[4,5] Darren Croton,[4,5]
Sofía A. Cora,[6,7] Eric Jullo,[8] Anatoly A. Klypin,[9,10] Masahiro Nagashima,[11] J. López Cacheiro,[12]
José Ruedas,[3] Masakazu A. R. Kobayashi[13,14] and Ryu Makiya[15,16]

[1]*Research Center for Space and Cosmic Evolution, Ehime University, 2-5, Bunkyo-cho, Matsuyama, Ehime 790-8577, Japan*
[2]*Digital Transformation Enhancement Council, Chiba University, 1-33, Yayoi-cho, Inage-ku, Chiba 263-8522, Japan*
[3]*Instituto de Astrofísica de Andalucía (CSIC), Glorieta de la Astronomía, E-18080 Granada, Spain*
[4]*Centre for Astrophysics & Supercomputing, Swinburne University of Technology, 1 Alfred St, Hawthorn, VIC 3122, Australia*
[5]*ARC Centre of Excellence for All Sky Astrophysics in 3 Dimensions (ASTRO 3D), Australia*
[6]*Instituto de Astrofísica de La Plata (CCT La Plata, CONICET, UNLP), Observatorio Astronómico, Paseo del Bosque, B1900FWA, La Plata, Argentina*
[7]*Facultad de Ciencias Astronómicas y Geofísicas, Universidad Nacional de La Plata (UNLP), Observatorio Astronómico, Paseo del Bosque, B1900FWA La Plata, Argentina*
[8]*Aix Marseille Univ, CNRS, CNES, LAM, F-13388 Marseille, France*
[9]*Astronomy Department, New Mexico State University, Las Cruces, NM 88001, USA*
[10]*Department of Astronomy, University of Virginia, Charlettesville, VA 22904, USA*
[11]*Faculty of Education, Bunkyo University, 3337 Minami-Ogishima, Koshigaya-shi, Saitama 343-8511, Japan*
[12]*Centro de Supercomputación de Galicia (CESGA), Avenida de Vigo, s/n Campus Sur, E-15705 Santiago de Compostel, Spain*
[13]*National Institute of Technology, 701-2 Higashiasakawa-machi, Hachioji, Tokyo 193-0834, Japan*
[14]*KOSEN-KMITL, 1st Chalongkrung Road, Ladkrabang, Bangkok 10520, Thailand*
[15]*Institute of Astronomy and Astrophysics, Academia Sinica, Astronomy-Mathematics Building, AS/NTU, No. 1, Section 4, Roosevelt Road, Taipei 10617, Taiwan*
[16]*Kavli Institute for the Physics and Mathematics of the Universe, Todai Institutes for Advanced Study, the University of Tokyo, Kashiwa 277-8583 (Kavli IPMU, WPI), Japan*

Accepted 2023 August 3. Received 2023 July 27; in original form 2022 July 29

ABSTRACT

Measurements of the luminosity function of active galactic nuclei (AGN) at high redshift ($z \gtrsim 6$) are expected to suffer from field-to-field variance, including cosmic and Poisson variances. Future surveys, such as those from the *Euclid* telescope and JWST, will also be affected by field variance. We use the Uchuu simulation, a state-of-the-art cosmological *N*-body simulation with 2.1 trillion particles in a volume of 25.7 Gpc^3, combined with a semi-analytic galaxy and AGN formation model, to generate the Uchuu–ν^2GC catalogue, publicly available, that allows us to investigate the field-to-field variance of the luminosity function of AGN. With this Uchuu–ν^2GC model, we quantify the cosmic variance as a function of survey area, AGN luminosity, and redshift. In general, cosmic variance decreases with increasing survey area and decreasing redshift. We find that at $z \sim 6 - 7$, the cosmic variance depends weakly on AGN luminosity. This is because the typical mass of dark matter haloes in which AGN reside does not significantly depend on luminosity. Due to the rarity of AGN, Poisson variance dominates the total field-to-field variance, especially for bright AGN. We also examine the effect of parameters related to galaxy formation physics on the field variance. We discuss uncertainties present in the estimation of the faint-end of the AGN luminosity function from recent observations, and extend this to make predictions for the expected number of AGN and their variance for upcoming observations with *Euclid*, JWST, and the Legacy Survey of Space and Time (LSST).

Key words: methods: numerical – catalogues – galaxies: formation – galaxies: nuclei – large-scale structure of Universe – cosmology: theory.

1 INTRODUCTION

Observations of the number density of galaxies and active galactic nuclei (AGN), and their redshift dependence across cosmic time, have yielded a number of important insights into their formation processes in a cosmological context. Our current knowledge has been advanced by comparing observations and theoretical predictions derived from semi-analytic models and cosmological hydrodynamical simulations (e.g. Somerville & Davé 2015). In particular, the AGN luminosity function (LF) is known to be shaped by various physical processes, such as triggers of gas accretion onto the black hole, the gas accretion rate, accretion disc states, the radiative efficiency, the AGN light curve, and their obscured (or observable) fraction (e.g. Hirschmann

---

★ E-mail: oogi@cosmos.phys.sci.ehime-u.ac.jp

Published by Oxford University Press on behalf of Royal Astronomical Society

et al. 2012; Fanidakis et al. 2012; Shirakata et al. 2019; Griffin et al. 2019). All these processes can be modelled and explored in detail.

However observations from surveys are limited by cosmic variance, and one must quantify this variance to properly constrain galaxy and AGN formation models. The faint-end of the AGN LF at $z \sim 6$ has non-negligible errors on the slope and normalization (e.g. Willott et al. 2010; Matsuoka et al. 2018). These uncertainties also affect the detectability of AGN and the design strategy for future AGN surveys and their instrument requirements; for example the kinds of future instruments needed, and the types of surveys targeting AGN that will better help nail down such uncertainties.

Similarly, measurements of the galaxy ultraviolet LF across the epoch of reionization (Bouwens et al. 2015; Livermore, Finkelstein & Lotz 2017) have large uncertainties at the faint-end (Atek et al. 2018; Ishigaki et al. 2018; Yue et al. 2018). And while data from new surveys and facilities, such as JWST (Gardner et al. 2006), *Euclid* (Laureijs et al. 2011), and the Legacy Survey of Space and Time (LSST) (LSST Science Collaboration 2009), will dramatically increase the volume of high-redshift ($z \gtrsim 6$) galaxy and AGN samples, a precise measurement of the LF will remain limited due to the inevitable finite survey volume. It is thus essential to quantify this uncertainty for current and future surveys and identify the required precision needed by them to accurately measure the relative galaxy and AGN contributions to cosmic reionization (Giallongo et al. 2019; Grazian et al. 2020).

A number of studies have theoretically evaluated the cosmic variance of galaxies at high redshift (e.g. Somerville et al. 2004; Trenti & Stiavelli 2008; Ogura et al. 2020; Bhowmick et al. 2020; Ucci et al. 2021). Ogura et al. (2020) used a semi-analytic model of galaxy and AGN formation, the New Numerical Galaxy Catalogue (ν^2GC; Makiya et al. 2016; Shirakata et al. 2019), to evaluate the cosmic variance of Hα emitters at $z = 0.4$. They also quantified how cosmic variance depends on survey volume. Bhowmick et al. (2020) used the large and high resolution cosmological hydrodynamical simulation, BLUETIDES (Feng et al. 2016), to investigate the cosmic variance of $z > 7$ galaxies. And Ucci et al. (2021) investigated the cosmic variance of high-z galaxies during the epoch of reionization, and how cosmic variance depends on the galaxy and AGN model parameters. Commonly, in such studies cosmic variance is evaluated using the two-point correlation function (e.g. Somerville et al. 2004; Trenti & Stiavelli 2008; Moster et al. 2011), advantageous for sparse populations, such as AGN, when limited to smaller volumes, as has been the case with simulations up until recently.

Theoretical work has also been done to predict the AGN population at $z \gtrsim 6$ using semi-analytic models (Ricarte & Natarajan 2018; Griffin et al. 2020; Piana et al. 2021) and cosmological hydrodynamical simulations (Feng et al. 2016; Waters et al. 2016; Habouzit et al. 2019; Marshall et al. 2020, 2021; Ni, Di Matteo & Feng 2021; Ni et al. 2020b – see also Amarantidis et al. (2019) for a compilation of predictions using such model). However, these studies have not examined the cosmic variance of the AGN LF due to their insufficient simulation box sizes.

In this paper, we explore the cosmic variance of AGN by using the semi-analytic model ν^2GC (Makiya et al. 2016; Shirakata et al. 2019). Specifically, we combine this model with the Uchuu simulation, a large cosmological dark matter N-body simulation (Ishiyama et al. 2021), from which we obtain the merger trees of dark matter haloes. Uchuu has an unprecedented box size of side length 2.0 h^{-1} Gpc with sufficient mass resolution to resolve the dwarf galaxy scale. This enables us to investigate various statistical properties of rare objects with low space densities, such as bright galaxies and AGN. This new Uchuu–ν^2GC galaxy and AGN catalogue is released to public along with this paper through the Skies and Universes website.[1] Taking advantage of its large comoving volume, we evaluate the cosmic variance of AGN by their direct counting, instead of using the two-point correlation function as in previous works (e.g. Somerville et al. 2004). We focus on AGN at $z \gtrsim 6$, mimicking the redshift range covered by upcoming JWST and *Euclid* AGN surveys, which will significantly increase the AGN statistics.

The remainder of this paper is organized as follows. In Section 2, we outline the semi-analytic model of galaxy and AGN formation used to generate our AGN statistics. The cosmic variance predicted from this model is presented in Section 3. In Section 4, we discuss the uncertainties in these predictions, and summarize our findings.

2 METHODS

2.1 The Uchuu simulation

A distinguishing feature of this study is the state-of-the art cosmological dark matter N-body simulation on which it is based, the Uchuu simulation (Ishiyama et al. 2021). The Uchuu simulation evolved an $12\,800^3$ dark matter (DM) particles within a box of side length 2.0 h^{-1} Gpc, resulting in a DM particle mass of $3.27 \times 10^8\, h^{-1}\,\mathrm{M}_{\odot}$. The cosmological parameters adopted by Uchuu are consistent with the latest results of the Planck satellite (Planck Collaboration 2020): $\Omega_0 = 0.3089$, $\Omega_\mathrm{b} = 0.0486$, $\lambda_0 = 0.6911$, $h = 0.6774$, $n_\mathrm{s} = 0.9667$, and $\sigma_8 = 0.8159$. Uchuu was performed with the code GREEM (Ishiyama, Fukushige & Makino 2009; Ishiyama, Nitadori & Makino 2012). A total of 50 snapshots of the simulation are stored between $z = 14$ and $z = 0$. DM haloes are identified in each snapshot with the ROCKSTAR phase-space halo finder (Behroozi, Wechsler & Wu 2013a). We use haloes with more than 40 particles, which corresponds to mass larger than $1.3 \times 10^{10}\, h^{-1}\,\mathrm{M}_{\odot}$. DM halo merger trees are constructed from the ROCKSTAR halo catalogue using a modified version of the CONSISTENT TREES code (Behroozi et al. 2013b). Further details of the Uchuu simulation and the post-processing steps are given in Ishiyama et al. (2021). The Uchuu DR1 data products are publicly available at the Skies & Universes website.[2]

2.2 The ν^2GC semi-analytic model

ν^2GC is a semi-analytic model of galaxy and AGN formation, and is an extension of the Numerical Galaxy Catalogue (νGC; Nagashima et al. 2005). The model runs on the DM halo merger trees obtained from high-resolution cosmological N-body simulations. Here, we use the merger trees from the Uchuu simulation described earlier, which allows us to assess the cosmic variance with direct object counts.

ν^2GC includes key baryonic processes for galaxy formation: radiative gas cooling and disc formation in DM haloes, star formation, supernova feedback, chemical enrichment, galaxy mergers, and disc instabilities, which trigger starbursts and lead to the growth of bulges and supermassive black holes (SMBHs), and AGN feedback. Further details of this galaxy formation model are given in Makiya et al. (2016) and Shirakata et al. (2019). Here, we briefly summarize the relevant physics for the current work, notably that related to AGN (see Shirakata et al. 2019; Oogi et al. 2020 for a more detailed description).

---

[1] http://www.skiesanduniverses.org

[2] http://www.skiesanduniverses.org/Simulations/Uchuu/

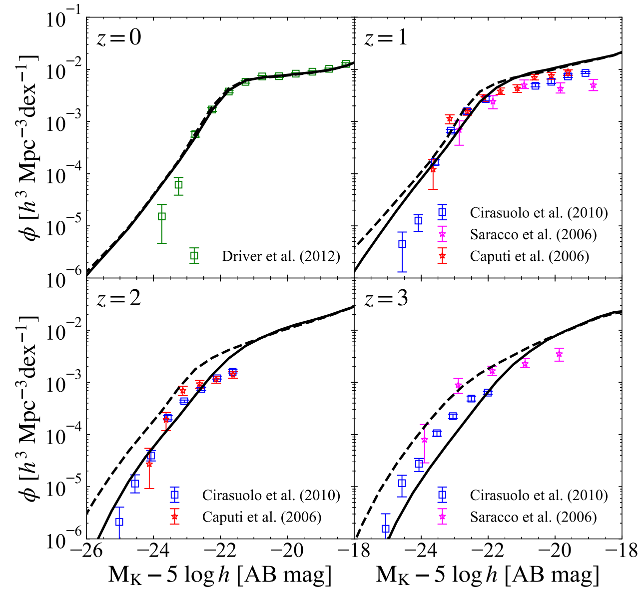

Figure 1. Rest-frame LFs in the *K* band at redshift 0, 1, 2, and 3. The solid and dashed lines show the Uchuu–ν^2GC LF with and without dust extinction, respectively. Open green squares at $z = 0$ are the observations from Driver et al. (2012), open red stars at $z = 1$ and 2 are from Caputi et al. (2006), open magenta stars at $z = 1$ and 3 are from Saracco et al. (2006), and open blue squares are from Cirasuolo et al. (2010).

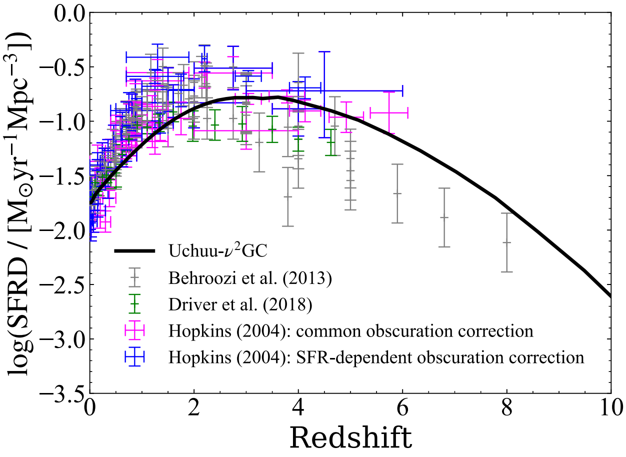

Figure 2. Cosmic SFR density as a function of redshift. The solid line is the result obtained from Uchuu–ν^2GC. Grey crosses with error bars are a compilation of observational estimates from Behroozi, Wechsler & Conroy (2013c). Green data are from Driver et al. (2018). Magenta (blue) data are from Hopkins (2004) with a common (SFR-dependent) obscuration correction. The model SFRs are converted to a Salpeter initial mass function (IMF) from Chabrier IMF by multiplying by a factor of 1.8.

In the model, SMBHs grow via mergers and disc instabilities that trigger starbursts, during which gas moves toward the central region of the galaxy and is accreted. In this paper, we focus on the disc instability process. The radius normalized by the disc scale radius, $R_{\rm gas}/r_{\rm ds}$, within which the gas migrates to the bulge, is determined as

$$\frac{R_{\rm gas}}{r_{\rm ds}} = (1 - f_{\rm g}) f_{\rm d} f_{\rm bar}, \tag{1}$$

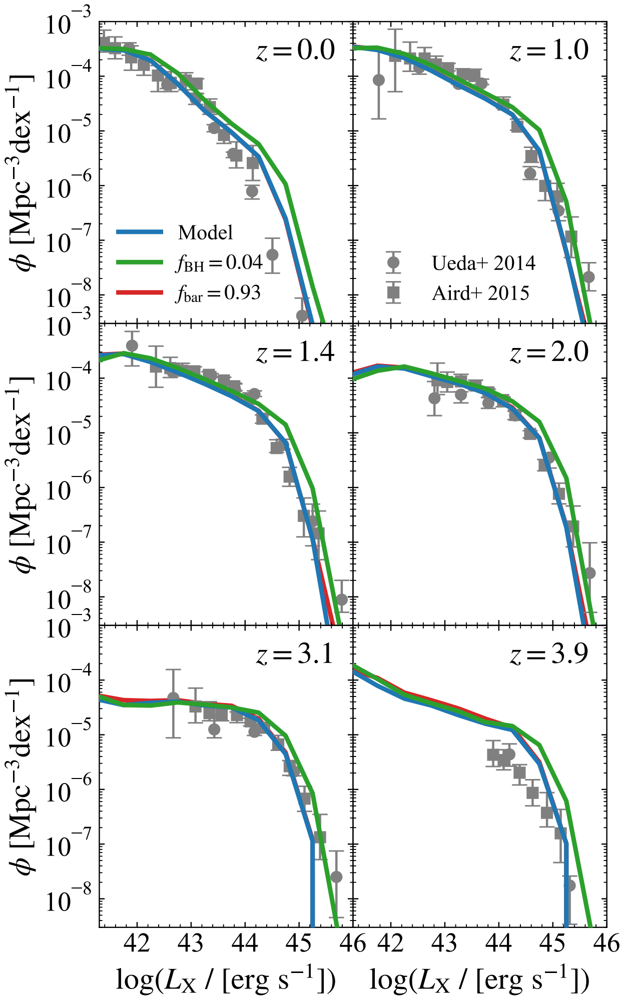

Figure 3. AGN hard X-ray LFs from $z = 0$ to $z = 4$. Blue solid lines show the result from Uchuu–ν^2GC. Grey data points with error bars show the observational results from Ueda et al. (2014) and Aird et al. (2015).

where $f_{\rm d}$ is the disc mass fraction of a galaxy, $f_{\rm g}$ is the gas mass fraction in the disc, and $f_{\rm bar}$ is a free parameter, which controls the strength of the disc instability. This formulation is motivated by the model of the merger induced gas accretion in Hopkins et al. (2009). Assuming an exponential surface density profile for the gas disc, the gas mass in the disc, which migrates to the bulge and is exhausted by a starburst, $\Delta M_{\rm dg,\,DI}$, is given by

$$\Delta M_{\rm dg,DI} = M_{\rm dg} \times \left\{ 1 - \left(1 + \frac{R_{\rm gas}}{r_{\rm ds}} \right) \exp(-R_{\rm gas}/r_{\rm ds}) \right\}, \tag{2}$$

where $M_{\rm dg}$ is the gas mass of the disc.

The accreted gas mass on to a SMBH, $\Delta M_{\rm BH}$, is given by

$$\Delta M_{\rm BH} = f_{\rm BH} \Delta M_{\rm star,burst}, \tag{3}$$

where $\Delta M_{\rm star,\,burst}$ is the stellar mass formed throughout a starburst. The parameter $f_{\rm BH}$ is set to 0.02 to match the observed correlation between the masses of host bulges and their SMBHs at $z = 0$ (McConnell & Ma 2013). The gas accretion rate is described by

$$\dot{M}_{\rm BH}(t) = \frac{\Delta M_{\rm BH}}{t_{\rm acc}} \exp\left(-\frac{t - t_{\rm start}}{t_{\rm acc}} \right), \tag{4}$$

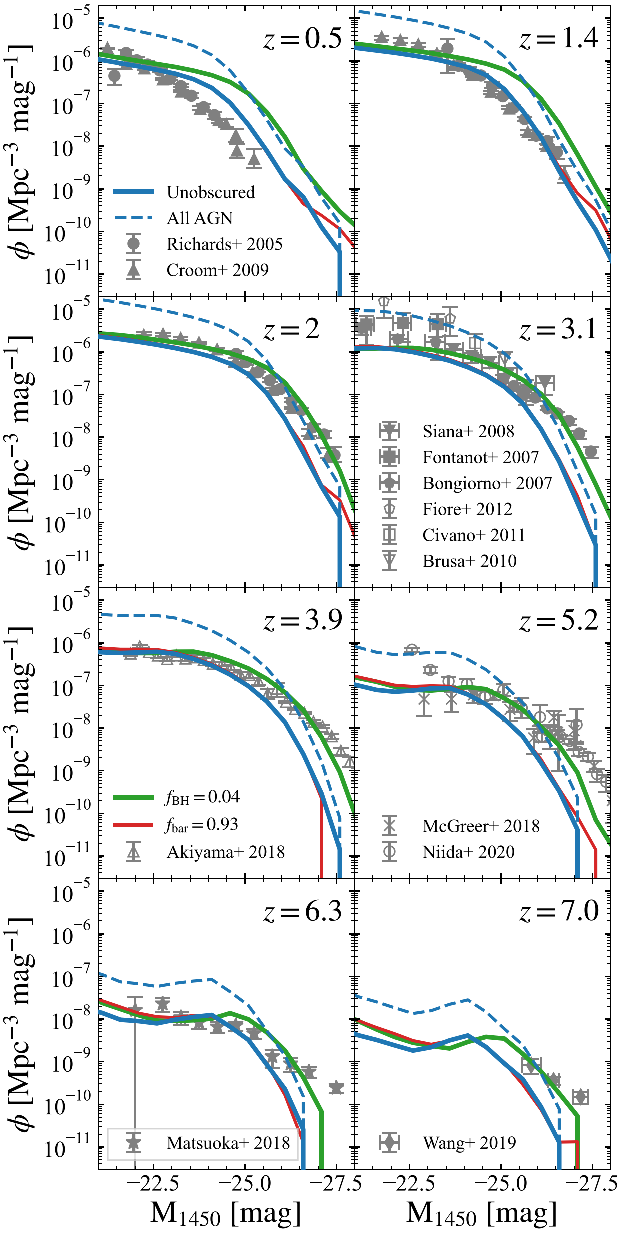

Figure 4. AGN UV LFs from $z = 0$ to $z = 7$. Blue solid lines show the result from Uchuu–ν^2GC. Blue dashed lines show the same but without dust obscuration, that is, the intrinsic AGN LF. Green (red) lines show the result of our model with $f_{\rm BH} = 0.04$ ($f_{\rm bar} = 0.93$). Grey data points with error bars show the observational results from Richards et al. (2005), Croom et al. (2009), Siana et al. (2008), Fontanot et al. (2007), Bongiorno et al. (2007), Fiore et al. (2012), Civano et al. (2011), Brusa et al. (2010), Akiyama et al. (2018), Niida et al. (2020), Matsuoka et al. (2018), and Wang et al. (2019).

where $t_{\rm acc}$ is the accretion time-scale and $t_{\rm start}$ is the start time of the accretion.

We assume that $t_{\rm acc}$ is determined by the loss of angular momentum of the accreted gas in the nuclear region, in addition to the dynamical time-scale of the host galaxy's bulge, $t_{\rm dyn,\,bulge}$:

$$t_{\rm acc} = \alpha_{\rm bulge} t_{\rm dyn,bulge} + t_{\rm loss}, \tag{5}$$

where $\alpha_{\rm bulge}$ is a free parameter, and $t_{\rm loss}$ is the time-scale for angular momentum loss (Shirakata et al. 2019). The parameter $\alpha_{\rm bulge}$ is set to 0.58 to ensure that the bright end of the AGN LF matches the observations (Ueda et al. 2014; Aird et al. 2015). In other words, the accretion rate of bright AGN is controlled by the dynamics of the host galaxy. The motivation for introducing $t_{\rm loss}$ is that the gas accretion rate should also be regulated by the physics that governs the dynamics of gas around the SMBH, as well as the dynamics of the host galaxy. We assume that $t_{\rm loss}$ depends both on the SMBH mass $M_{\rm BH}$ and $\Delta M_{\rm BH}$:

$$t_{\rm loss} = t_{\rm loss,0} \left(\frac{M_{\rm BH}}{{\rm M}_\odot}\right)^{\gamma_{\rm BH}} \left(\frac{\Delta M_{\rm BH}}{{\rm M}_\odot}\right)^{\gamma_{\rm gas}}, \tag{6}$$

where $t_{\rm loss,\,0}$, $\gamma_{\rm BH}$, and $\gamma_{\rm gas}$ are free parameters, and are set to 1 Gyr, 3.5, and −4.0, respectively. Based on this model, the dominant term in $t_{\rm acc}$ is $t_{\rm loss}$ for most AGN with low-luminosity and/or at low redshifts, as shown in Shirakata et al. (2019) (see their Fig. 7). Due to this term, the number density of AGN with low luminosity increases at $z \lesssim 1.5$.

The gas accretion on to a SMBH leads to AGN activity. The Eddington luminosity is defined as $L_{\rm Edd} \equiv 4\pi G M_{\rm BH} m_{\rm p} c/\sigma_{\rm T}$, where c is the speed of light, G is the gravitational constant, $m_{\rm p}$ is the proton mass, and $\sigma_{\rm T}$ is the Thomson scattering cross-section. With this, the Eddington accretion rate is defined as $\dot{M}_{\rm Edd} \equiv L_{\rm Edd}/c^2$. Taking into account the effect of 'photon trapping' (e.g. Ohsuga et al. 2005) when a super-Eddington accretion occurs, we adopt the following relation for the AGN bolometric luminosity, $L_{\rm bol}$, normalized by the Eddington luminosity, $\lambda_{\rm Edd} \equiv L_{\rm bol}/L_{\rm Edd}$:

$$\lambda_{\rm Edd} = \left[\frac{1}{1 + 3.5\{1 + \tanh(\log(\dot{m}/\dot{m}_{\rm crit}))\}} + \frac{\dot{m}_{\rm crit}}{\dot{m}}\right]^{-1}, \tag{7}$$

where $\dot{m}$ is the accretion rate normalized by the Eddington rate, $\dot{m} \equiv \dot{M}_{\rm BH}/\dot{M}_{\rm Edd}$. This form is based on Kawaguchi (2003). This kind of suppression of $\lambda_{\rm Edd}$ at high $\dot{m}$ is described by the slim disc solution (e.g. Mineshige et al. 2000). We set $\dot{m}_{\rm crit} = 10.0$ (Shirakata et al. 2019). Further, we use the bolometric correction from Marconi et al. (2004) to obtain the hard X-ray (2–10 keV) and B-band luminosity of AGN. We then use

$$M_{\rm UV} = M_B + 0.85, \tag{8}$$

to derive the UV magnitude. This equation is obtained by assuming the template SED presented in Kawaguchi, Shimura & Mineshige (2001). For comparison, we also use Duras et al. (2020) bolometric correction to obtain the AGN UV LF in Section 4.

Using the fiducial parameters in Shirakata et al. (2019), our new model with the Uchuu simulation reproduces a number of key observed galaxy statistics, including the local mass function of neutral hydrogen, the local SMBH mass function, and the high-z K-band LF up to $z \sim 3$ (Makiya et al. 2016; Shirakata et al. 2019), except for the faint end of the K-band and r-band LFs of local galaxies. The model slightly under-predicts the number densities at magnitudes fainter than the M_* of these LFs. We recalibrate every parameter by hand and find that the weakening the strength of the supernova (SN) feedback makes the fit better without changing any other statistics significantly. For this we take $\alpha_{\rm hot} = 3.62$ instead of 3.92 in Shirakata et al. (2019). Our model also reproduces local scaling relations, such as the Tully–Fisher relation, the size – magnitude relation of spiral galaxies, and the relation between bulge and black hole mass. ν^2GC is a mature model, and has already been used in the study of SMBHs and AGN (Enoki et al. 2014; Oogi et al. 2016, 2017; Shirakata et al. 2016).

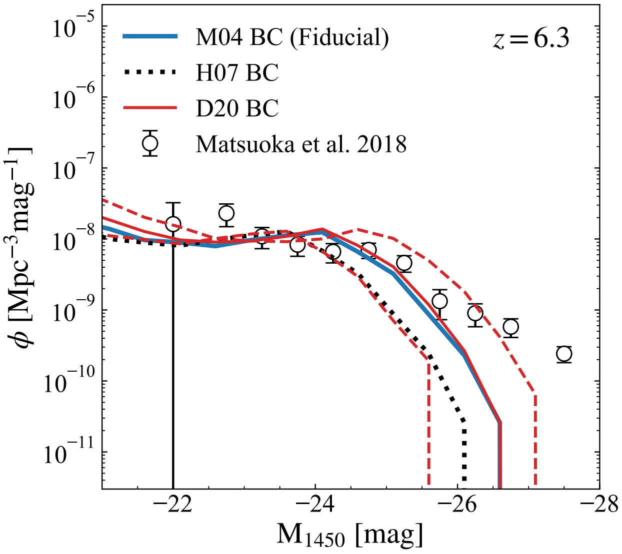

Figure 5. AGN UV LFs at $z = 6.3$ with different optical bolometric corrections, which are the ratios between the bolometric luminosity and the luminosity in the 4400 Å band. The blue line shows the result from Marconi et al. (2004), which we adopt in our fiducial model. The black dotted line shows the result of Hopkins, Richards & Hernquist (2007). Red lines show the the result of Duras et al. (2020): the the best fit (solid) and the scatter (dashed).

2.3 Uchuu–ν^2GC galaxy and AGN statistics

First, we briefly present our galaxy statistics to set a baseline for the subsequent AGN results. The ν^2GC model now runs on the Uchuu simulation, however previous work instead used the ν^2GC simulation (Ishiyama et al. 2015). This difference required us to recalibrate the model parameters described in Section 2.2. The resulting model parameter values are identical to Shirakata et al. (2019), except for $\alpha_{\rm hot} = 3.62$ instead of 3.92.

In Fig. 1, we show the K-band galaxy LFs at $z = 0$, 1, 2, and 3. We compare our results with relevant observational data at these redshifts, as labelled. The model K-band LF shows good agreement with the observations up to $z = 3$, although the effect of dust attenuation becomes too strong at $z = 3$. This over-attenuation may be partly due to the estimation of galaxy sizes, which are used to calculate dust surface densities to determine the attenuation in ν^2GC (Makiya et al. 2016). A similar tendency to this over-attenuation on the K band has been seen in other semi-analytic models (see fig. 8 in Somerville et al. 2012 and fig. 7 in Lacey et al. 2016). We will address the treatment of dust attenuation in future work. We note that some other studies have also explored the K-band LF with semi-analytic models (e.g. Henriques et al. 2011; Lagos et al. 2019).

Fig. 2 shows the cosmic star formation rate (SFR) density. The overall shape of the redshift evolution is almost consistent with observations, while our model slightly under-predicts the SFR density at $z \sim 1 - 2$. Exploring the reasons for this in the model, we find that disc instabilities strongly shape our SFR density at $z \lesssim 3$. With them, central black hole growth is enhanced relative to the model without disc instabilities, and the resultant AGN feedback suppresses the SFR density. Other statistics in the model, such as the black hole mass function in the local universe and the black hole mass–bulge mass relation, are also in well agreement with recent observational data. Further model galaxy results can be found in Makiya et al. (2016) and Shirakata et al. (2019).

The further set of figures illustrate how Uchuu–ν^2GC reproduces the observed LF of AGN over a wide redshift range, $0 < z < 6$ (Shirakata et al. 2019). Fig. 3 compares the intrinsic AGN hard X-ray LFs of Uchuu–ν^2GC and observations from $z = 0$ to $z = 4$. Fig. 4 shows the AGN UV LFs from $z = 0$ to $z = 7$. While our model broadly reproduces the observed AGN UV LF at $\mathrm{M}_{1450} \gtrsim -25$, it under-predicts the bright-end. Figs 3 and 4 also show the results of two model variants, one with $f_{\rm BH} = 0.04$ and one with $f_{\rm bar} = 0.93$ for comparison. It seems that the model with $f_{\rm BH} = 0.04$ is in more agreement with the observations at $z \gtrsim 2$. Since our fiducial model assumes that $f_{\rm BH}$ is redshift independent, we have set $f_{\rm BH} = 0.02$ to match the LFs at $z < 2$ and the observed correlation between the masses of host bulges and their SMBHs at $z = 0$ (McConnell & Ma 2013). We have also verified that the predicted two-point correlation function of AGN is also consistent with current observations (Oogi et al. 2020).

In this paper, we have assumed the empirical SED of AGN which follows a power law in the wavelength range from UV to infrared (Marconi et al. 2004) as well as their bolometric correction. Indeed, the UV magnitude of AGN depends on bolometric correction, which can introduce a large uncertainty in the prediction of the LF. We have used two different bolometric corrections from Hopkins et al. (2007) and Duras et al. (2020) to address its effect on the predicted AGN UV LF. This revealed how the bolometric correction affects the bright end of the LF. In Fig. 5, we show the effect of the bolometric correction on the AGN LF at $z = 6.3$. The normalization of the bright end varies by ~1 dex within the scatter found by Duras et al. (2020). Taking into account the scatter of the bolometric correction, the uncertainties of this correction are larger than those derived for the runs with the different parameters. This leads to different expected numbers of bright AGN for future surveys. Future work will further investigate the impact of bolometric correction on the AGN SED and the resulting detectable number of AGN.

In this work, we focus on AGN with hard X-ray luminosity $L_{\rm 2\text{-}10keV}$ larger than 10^{41} erg s^{-1}, which corresponds to a bolometric luminosity $L_{\rm bol} \sim 40^{42}$ erg s^{-1}. The corresponding UV magnitude depends on the dust obscuration. To account for dust obscuration, we use the 'observable fraction' introduced by Shirakata et al. (2019). For intrinsic AGN UV LFs obtained with our model, Shirakata et al. (2019) have empirically determined the observable fraction that fits the observed AGN UV LF (see Shirakata et al. 2019 and their equation (21) for details).

2.4 Quantification of cosmic variance

Here, we describe how we quantify the cosmic variance of the AGN samples in our Uchuu–ν^2GC catalogue. The *relative* cosmic variance $\sigma_{\rm cv}$ can be defined as follows (Somerville et al. 2004; Bhowmick et al. 2020)

$$\sigma_{\rm cv}^2 = \frac{\langle N^2 \rangle - \langle N \rangle^2 - \langle N \rangle}{\langle N \rangle^2}, \qquad (9)$$

where N is the number of AGN in each subvolume and $\langle N \rangle$ is the mean number of AGN across all subvolumes. The first two terms in equation (9) represent the total field-to-field variance $\sigma_{\rm tot}^2$ which includes the contribution from the cosmic and Poisson variances, following the convention in Bhowmick et al. (2020). The third term represents the Poisson variance which is subtracted to obtain $\sigma_{\rm cv}$.

To evaluate $\sigma_{\rm cv}$, a procedure using the two-point correlation function is usually used (e.g. Somerville et al. 2004; Trenti & Stiavelli 2008; Moster et al. 2011). Bhowmick et al. (2020) have primarily used this method to determine $\sigma_{\rm cv}$ for $z > 7$ galaxies.

Table 1. Summary of the number of Uchuu–ν^2GC subvolumes corresponding to different survey sizes given the redshift width $\Delta z = 1$.

Survey area (deg^2)	Number of subvolumes					
Redshift	3.93	5.15	5.72	6.34	7.03	7.78
0.01	215 296	220 500	249 696	274 428	294 912	311 364
0.1	21 316	21 780	24 576	26 908	28 800	30 276
1.0	2116	2205	2400	2527	2888	2916
10.0	196	180	216	252	288	225
30.0	64	45	54	63	72	81
80.0	16	20	24	28	32	36

Table 2. Summary of the comoving lengths (in units of h^{-1}Mpc) corresponding to different Uchuu–ν^2GC survey sizes given the redshift width $\Delta z = 1$.

Survey area (deg^2)	Comoving length (h^{-1} Mpc)							
Redshift	3.93	5.15	5.72	6.34	7.03	7.78	8.58	9.48
0.01	8.6	9.5	9.8	10.1	10.4	10.7	11.0	11.3
0.1	27.3	30.1	31.1	32.1	33.0	34.0	34.8	35.7
1.0	86.2	95.0	98.3	101.4	104.5	107.4	110.1	112.7
10.0	272.6	300.6	310.9	320.8	330.3	339.5	348.1	356.5
30.0	472.2	520.6	538.4	555.6	572.1	558.0	602.9	617.5
80.0	711.1	850.1	879.3	907.2	934.2	960.3	984.5	1008.0
Redshift width								
$\Delta z = 1$	491.048	353.007	309.415	271.168	237.295	207.421	182.031	158.959

In this paper, we determine $\sigma_{\rm cv}$ by directly computing $\langle N\rangle$ and $\langle N^2\rangle$ from the AGN sample in subvolumes, taking advantage of the Uchuu simulation's large volume. Considering the areas of future surveys from telescopes such as JWST (~46 arcmin^2 and ~190 arcmin^2), and Euclid-deep (~40 deg^2), the Uchuu–ν^2GC volume is large enough to extract a number of independent AGN subvolume samples, needed for calculating the cosmic variance.

In this study, we use a single snapshot to evaluate the cosmic variance. choosing the z-axis of the simulation box, to represent the redshift width of mock surveys. Table 1 describes the subvolumes extracted having survey area A and redshift width Δz. We focus on redshifts $z = 5.72, 6.34, 7.03, 7.78, 8.58$, and 9.48, which correspond to the Uchuu snapshots. For each snapshot with redshift $z_{\rm i}$, we consider the comoving length corresponding $\Delta z = 1$ centred on z_i, and extract it along with the z-axis direction of the simulation box. We then extract the survey areas $A = 0.01, 0.1, 1, 10, 30$, and 80 deg^2 which have a square geometry with side-length corresponding to $\sqrt{A}$ in the $x - y$ plane of the simulation box. We convert degrees to the comoving lengths at each redshift z_i. Table 2 shows the comoving lengths of the subvolumes obtained from our simulation box for each survey area and redshift.

In addition to the cuboid geometry described earlier, we also consider a cubic geometry. This is because previous studies have shown that the survey geometry affects the cosmic variance of the galaxy LF (Moster et al. 2011; Bhowmick et al. 2020). For the cubic geometry, we extract cubes with side length $L_{\rm eff}(= V_{\rm eff}^{1/3})$, where $V_{\rm eff}$ is a survey volume corresponding to the cuboid geometry. We test the effect of geometry on the total field-to-field variance in Section 3.4.

3 COSMIC VARIANCE OF AGN

3.1 AGN LF in each subvolume

First, in Fig. 6 we present AGN hard X-ray LFs for different survey areas: 0.01, 0.1, 1, 10, 30, and 80 deg^2 from $z = 3.9$ to 7.8. The shaded regions and bounding lines show $\langle N\rangle(1 \pm \sigma_{\rm tot})$, where $\sigma_{\rm tot}$ is the total field-to-field variance. In the case of a 1 deg^2 area, the faint end, $\log{(L_{\rm X}/{\rm erg\,s^{-1}})} \lesssim 42$, of the LF has a scatter of ~0.3 and ~0.5 dex at $z = 5.7$ and $z = 7.0$, respectively. The bright end, $\log{(L_{\rm X}/{\rm erg\,s^{-1}})} \gtrsim 44$, is noisy due to Poisson variance. The spread in the LF decreases with increasing survey area. For 30 and 80 deg^2 surveys, the LFs converge to the LF obtained from the full volume of the Uchuu simulation box, $(2\,h^{-1}\,{\rm Gpc})^3$, except at the bright end. As expected given the reduced number of AGN, the scatter is larger at higher redshift in every survey area.

Fig. 7 shows the AGN UV LFs in different survey areas: 1, 10, 30, and 80 deg^2 from $z = 3.9$ to 7.8. While the faint end ($M_{1450} \gtrsim -22$) can be constrained by a 1 deg^2 survey (with $\Delta z \sim 1$) at $z \leq 5.7$, the brighter end cannot, at all redshifts investigated. Using a 10 (30) deg^2 survey, the LFs for $M_{1450} \gtrsim -24$ can be constrained within 0.3 dex up to $z = 6.3$ (7.0). At $z = 7.8$, the AGN LF is significantly affected by field variance and cannot be constrained by a 30 deg^2 or smaller survey. At this redshift for the 80 deg^2 survey, the LFs at $M_{1450} \sim -24$ can be constrained within 0.3 dex. Our results show that the AGN UV LF at $M_{1450} \lesssim -26$ is unconstrained by anything smaller than a 80 deg^2 survey.

3.2 Dependence of the cosmic variance on the survey area

Fig. 8 summarizes the measured cosmic variance of AGN using $\sigma_{\rm cv}$ as a function of survey area. Each panel corresponds to a different redshift from $z = 3.9$ to $z = 7.8$, and shows five luminosity ranges. As seen by the LFs in Fig. 6, $\sigma_{\rm cv}$ decreases with increasing survey area for almost all luminosity ranges. The decreasing trend weakens at high redshift. $\sigma_{\rm cv}$ ranges from 3×10^{-3} to $\gtrsim 0.1$ depending on AGN luminosity and redshift.

The dependence of cosmic variance on survey area is fitted by a power-law function

$$\sigma_{\rm cv} = \Sigma\ \left(A/{\rm deg}^2\right)^{\alpha}, \tag{10}$$

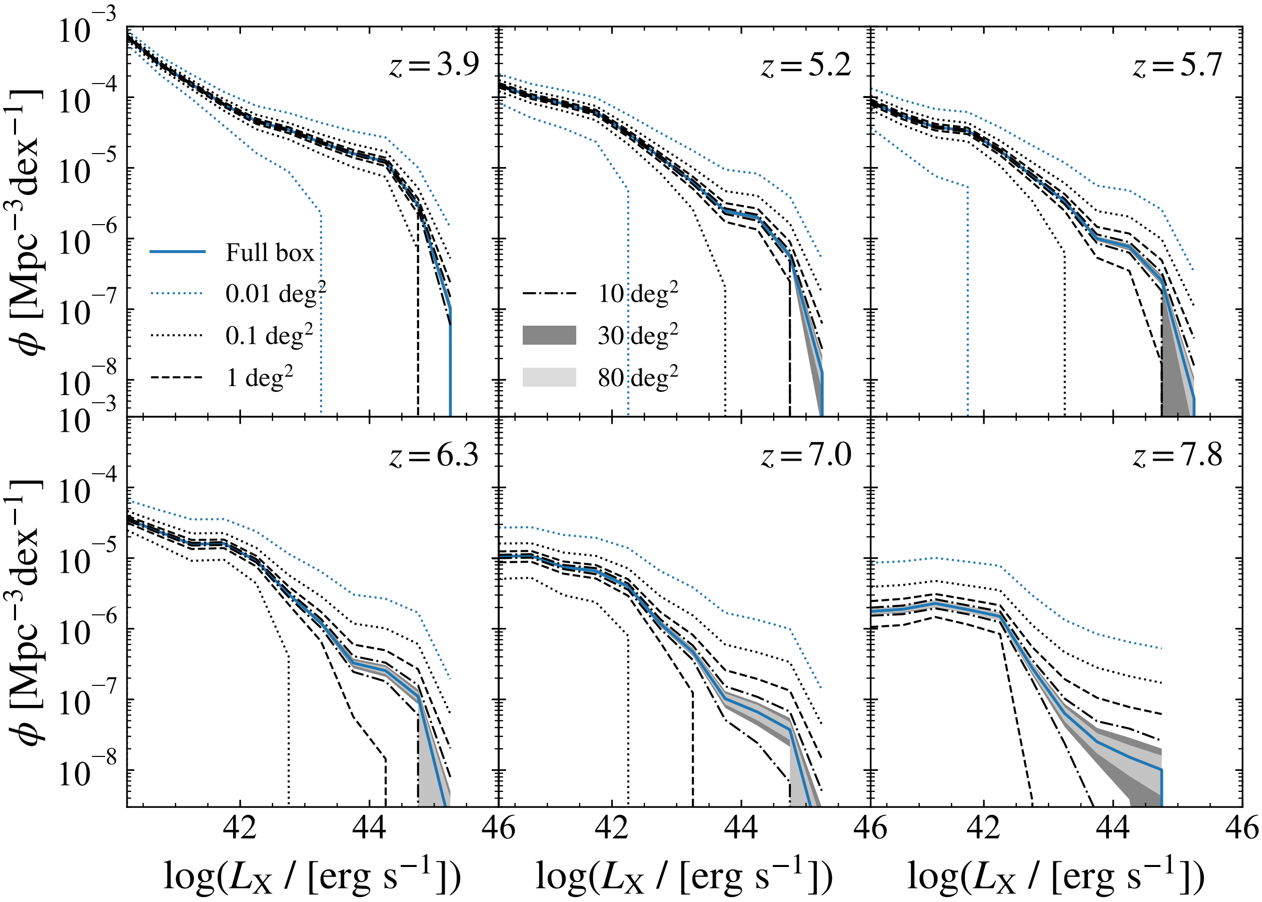

Figure 6. AGN hard X-ray LFs from Uchuu–ν^2GC for various survey areas (0.01, 0.1, 1, 10, 30, and 80 deg^2) from $z = 3.9$ to $z = 7.8$. The blue solid line in each panel shows the LF obtained from the full volume of the Uchuu simulation box, $(2\,h^{-1}\,\mathrm{Gpc})^3$. Dashed and dot-dashed lines depict the total field-to-field variance of the LF with 1 and 10 deg^2 survey areas. Light grey and dark grey regions depict those with 30 and 80 deg^2 survey areas, respectively.

where Σ is the normalization and α represents the slope of the power law. This is the same form as the one presented by Bhowmick et al. (2020). Table 3 summarizes the best-fitting values of Σ and α using the least-squares method for the hard X-ray LFs. Overall, the slope α ranges between ∼0.5 and ∼0.1. These values are roughly consistent with the results of Bhowmick et al. (2020) for $z > 7$ galaxies in the BLUETIDES simulation.

3.3 Dependence of the cosmic variance on the AGN luminosity and redshift

Further, we examine the luminosity dependence of cosmic variance in our model. Fig. 9 shows the cosmic variance for different survey areas as a function of AGN luminosity. From $z = 3.9$ to 6.3, $\sigma_{\rm cv}$ only depends weakly on AGN luminosity, in particular for small survey areas (0.01 and 0.1 deg^2). This is because the typical DM halo mass in which AGN reside does not monotonically rise with increasing luminosity (Oogi et al. 2020). Our result is consistent with the weak luminosity dependence of the observed quasar clustering (e.g. Croom et al. 2005; Myers et al. 2007; Shen et al. 2007; Padmanabhan et al. 2009; Ross et al. 2009; Krolewski & Eisenstein 2015). Although the weak luminosity dependence may be due to the limited luminosity range currently probed (e.g. White et al. 2012), He et al. (2018) have not found any significant luminosity dependence of the quasar clustering down to the UV magnitude $\mathrm{M}_{1450} \sim -22$ at $z \sim 4$. This lack of the luminosity dependence is in contrast to the results of $\sigma_{\rm cv}$ for $z > 7.5$ galaxies shown by Bhowmick et al. (2020). For their galaxy sample, brighter galaxies are more strongly clustered.

In Fig. 9, we also see the redshift dependence of $\sigma_{\rm cv}$. For low-luminosity AGN with $\log\,(L_{\rm X}/\mathrm{erg\,s^{-1}}) \simeq 41$, $\sigma_{\rm cv}$ gradually increases from $z = 3.9$ to $z = 7.8$ by a factor of 3–20, depending on the survey area. This trend is partly due to the change in the comoving survey volume. If we assume a fixed survey area and redshift depth, the corresponding comoving survey volume decreases with redshift. This is because the fixed redshift interval is chosen ($\Delta z = 1$ in this paper). For example, for a 80 deg^2 survey area and $\Delta z = 1$, the comoving survey volume is 0.939 Gpc^3 at $z = 3.9$, while it is 0.615 Gpc^3 at $z = 7.8$, as can be seen from Table 2. Another possible reason for the redshift dependence is the change in AGN clustering, which leads to the change in $\sigma_{\rm cv}$. For high-luminosity AGN with $\log\,(L_{\rm X}/\mathrm{erg\,s^{-1}}) \simeq 44$, $\sigma_{\rm cv}$ also increases from $z = 3.9$ to $z = 7.0$ by a factor of 5–15, although the trend is noisy due to the finite number density.

Fig. 10 shows the ratio of the cosmic variance to Poisson variance. In the case of 1 deg^2 and smaller survey areas, the Poisson variance dominates the total variance at all redshifts. In the case of 30 and 80 deg^2, the cosmic variance dominates for lower-luminosity AGN with $\log\,(L_{\rm X}/\mathrm{erg\,s^{-1}}) \lesssim 42$, while the Poisson variance increases for higher-luminosity AGN. This trend weakens at $z \gtrsim 7$. This is because our model predicts the LF with a flatter faint end slope at

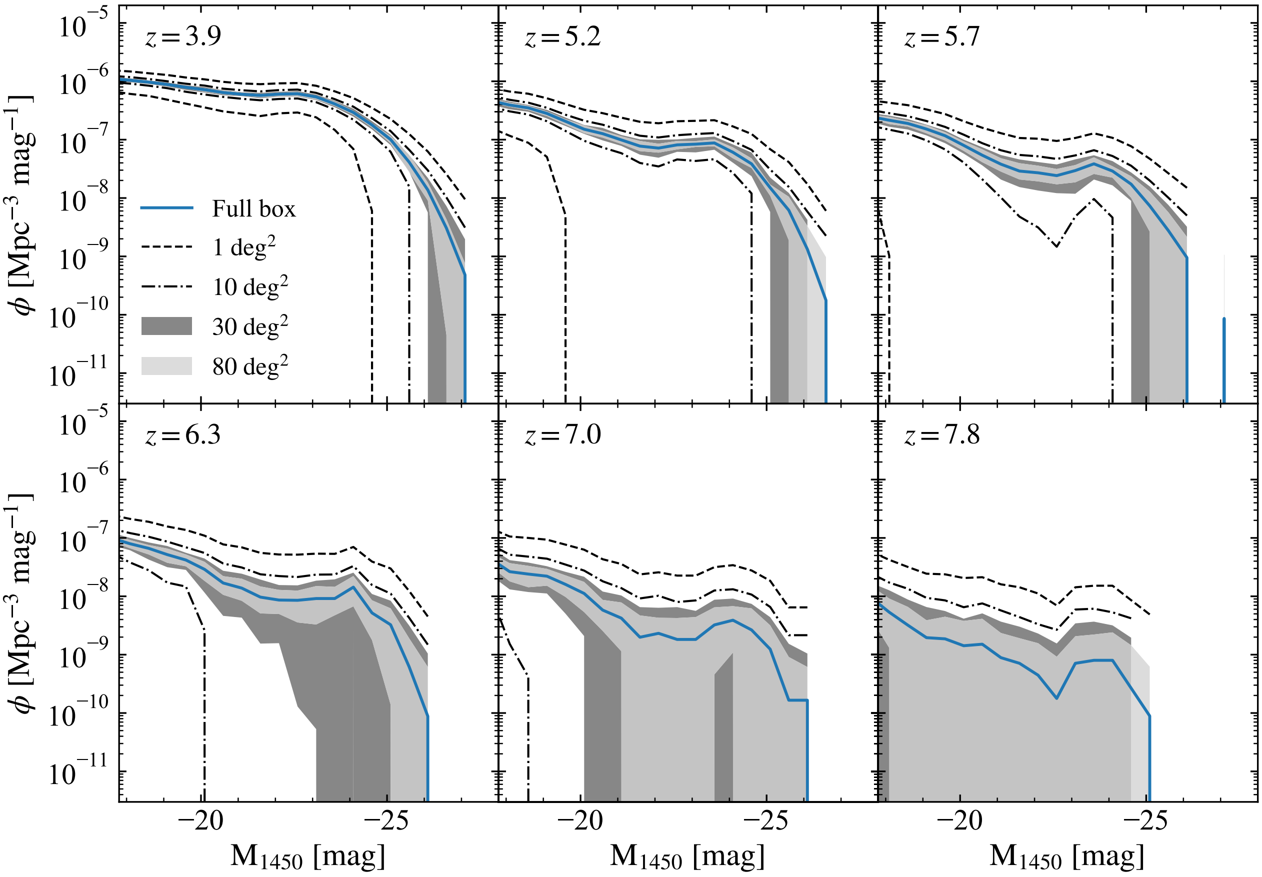

Figure 7. Same as Fig. 6, but for AGN UV LFs.

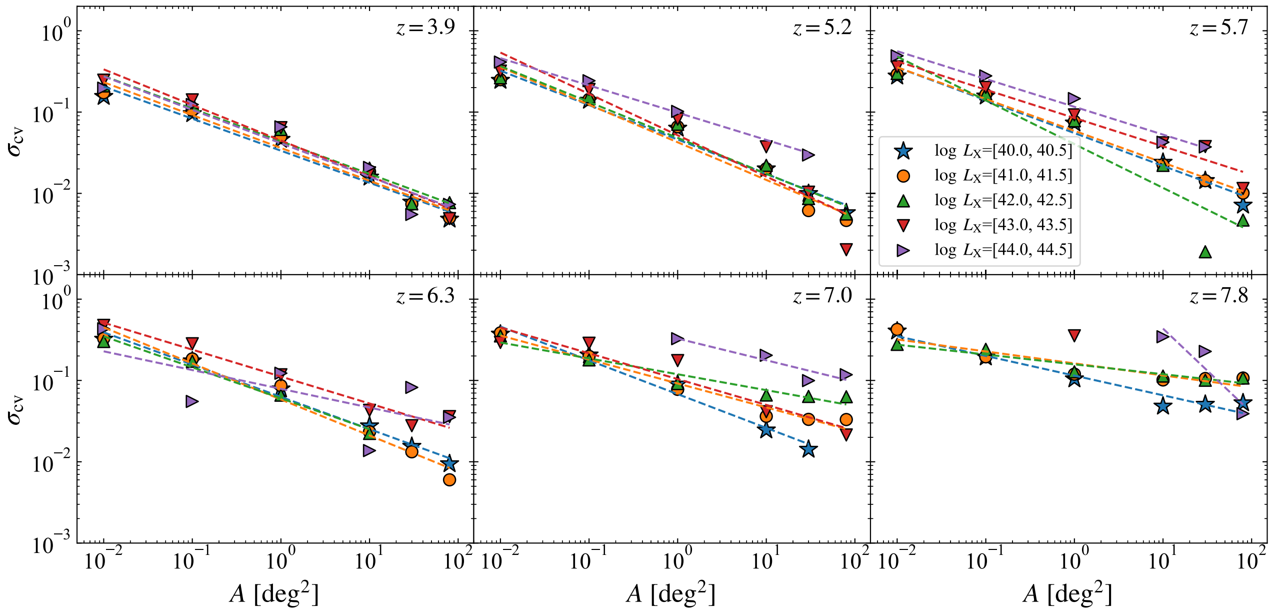

Figure 8. Cosmic variance as a function of survey area A for AGN samples with four luminosity ranges, $\log{(L_X/\mathrm{erg\ s^{-1}})} = [40.0, 40.5]$ (blue), [41.0, 41.5] (orange), [42.0, 42.5] (green), [43.0, 43.5] (red), and [44.0, 44.5] (purple), at different redshifts. The comoving length of the line of sight for each survey area is shown in Table 2.

Table 3. Results of power-law fits to the cosmic variance of AGN hard X-ray LFs obtained from equation (10).

$L_{\rm X}$	z	α	Σ $(\times 10^{-3})$
40.25	3.9	−0.39	33.48
41.25	3.9	−0.40	36.22
42.25	3.9	−0.40	43.74
43.25	3.9	−0.44	44.70
44.25	3.9	−0.41	41.34
40.25	5.2	−0.42	45.96
41.25	5.2	−0.46	42.50
42.25	5.2	−0.44	48.18
43.25	5.2	−0.51	51.91
44.25	5.2	−0.34	98.33
40.25	5.7	−0.40	55.18
41.25	5.7	−0.39	58.77
42.25	5.7	−0.54	40.34
43.25	5.7	−0.35	84.59
44.25	5.7	−0.34	116.1
40.25	6.3	−0.40	62.84
41.25	6.3	−0.44	58.41
42.25	6.3	−0.38	60.31
43.25	6.3	−0.33	111.6
44.25	6.3	−0.23	78.93
40.25	7.0	−0.42	67.89
41.25	7.0	−0.29	91.85
42.25	7.0	−0.20	119.2
43.25	7.0	−0.32	104.0
44.25	7.0	−0.27	327.5
40.25	7.8	−0.24	114.7
41.25	7.8	−0.15	162.1
42.25	7.8	−0.12	157.8
43.25	7.8	–	–
44.25	7.8	−1.03	4703

these redshifts compared to the lower redshifts (see Fig. 6). In other words, the AGN number density does not depend significantly on the luminosity in $L_{\rm X} \lesssim 10^{42}\,{\rm erg\,s^{-1}}$ at $z \gtrsim 7$. In this luminosity range, the Poisson variance is comparable to the cosmic variance, and there is no clear trend with luminosity.

It is important to remember that our estimates of the cosmic variance can be affected by uncertainties in the galaxy and AGN formation physics. Here, we investigate the effects of SMBH and AGN formation parameters on the total field-to-field variance. We focus on two model parameters, $f_{\rm BH}$ and $f_{\rm bar}$. These parameters change the amount of mass growth for each SMBH (see Section 2 and Shirakata et al. 2019). While the degree of the variance at the bright end of the LF is slightly different between the two models, the faint ends have similar variance. We will compare the results of the three variants of the model in Section 3.5.

3.4 Expected variance in current and future surveys

Our extremely large Uchuu–ν^2GC volume enables us to evaluate the expected field variance for existing and future LF surveys. In this subsection, we focus on the faint end of the AGN UV LF ($M_{\rm UV} \gtrsim -23$), because this is of importance for studies on the contribution of AGN to reionization (Giallongo et al. 2019; Grazian et al. 2020). Fig. 11 shows the total field-to-field variance $\sigma_{\rm tot}$ (the first two terms in equation (9)), of the faint end of AGN UV LF for several luminosity ranges as a function of effective box size $L_{\rm eff}$, corresponding to different effective survey volumes $V_{\rm eff}$. We again consider two types of geometries: cubic and cuboid (see Section 2.4); solid lines correspond to the cubic geometry, while dashed lines correspond to the cuboid geometry.

As expected, $\sigma_{\rm tot}$ decreases with $V_{\rm eff}$, like the survey area dependence in Fig. 8. The variances $\sigma_{\rm tot}$ of different magnitudes are not significantly different in this magnitude range. $\sigma_{\rm tot}$ increases with redshift. Our results also show that $\sigma_{\rm tot}$ only weakly depends on survey geometry. This may be because the Poisson variance dominates $\sigma_{\rm tot}$ in the case of AGN, in contrast to what occurs for galaxies.

We also compare our predictions with current observations in Fig. 11. First, from Akiyama et al. (2018) the $V_{\rm eff}$ of their AGN LF at $z \simeq 4$ is 0.34 (0.63) Gpc^3 for the magnitude bin of $M_{1450} = -21.875\,(-22.125)$. At these luminosity ranges, they have estimated the uncertainty of the LF to be ∼0.14 (0.09). For the same luminosity and redshift range, our estimate of the LF scatter, $\sigma_{\rm tot} \simeq 0.11$ (0.08), is consistent with their values. Secondly, for Niida et al. (2020) the $V_{\rm eff}$ at $z \simeq 5$ is 0.29 (0.33) Gpc^3 for the magnitude bin of $M_{1450} = -22.57\,(-23.07)$, and their corresponding uncertainty is ∼0.1 (∼0.2). In our analysis, $\sigma_{\rm tot} \simeq 0.24$ (0.35) at the same luminosity and redshift range. Our result is consistent within a factor of two. Finally, for Matsuoka et al. (2018) the $V_{\rm eff}$ at $z \simeq 6$ is 0.062 (0.694) Gpc^3 for the magnitude bin of $M_{1450} = -22.0\,(-22.75)$, and their corresponding uncertainty is ∼1 (∼0.35). In our analysis, $\sigma_{\rm tot} \simeq 2.0$ ($\simeq 0.5$), again consistent to their observational estimate within a factor of two.

Furthermore, Fig. 11 shows our predicted uncertainty for LFs that can be obtained from future surveys. For example, at $z = 7.8$ (7.0), $V_{\rm eff} \gtrsim 2$ (0.8) Gpc^3 is required to suppress the uncertainty to $\sigma_{\rm tot} \lesssim 1$. This relation between $L_{\rm eff}$ and $\sigma_{\rm tot}$ is needed if one would like to know the required survey area to constrain the AGN LF at a desired level.

3.5 Predictions of AGN LFs for upcoming surveys

Telescopes with new instruments, like those onboard the JWST and *Euclid* spacecrafts, and the LSST camera on the Vera Rubin telescope, can expand our understanding of the statistics of high-redshift AGN. To help guide our exploration of the AGN using these new facilities, we present predictions of the AGN LF and expected numbers that will be discovered by future surveys.

JWST, launched on December 2021, carries onboard the NIRCam instrument observing across the wavelength range 0.7–5 μm. With the NIRCam F200W filter it will measure AGN radiation at $z \geq 7$ in the rest-frame ultraviolet and optical wavelengths. Importantly, this radiation is expected to be less affected by the absorption of the inter-galactic medium. To derive the magnitude in the JWST bands, we convolve the spectral energy distribution (SED) for each AGN with the filter response functions in a set of NIRCam filters.[3] For an AGN SED, we assume the empirical SED which follows a power law in the wavelength range from UV to infrared (Marconi et al. 2004) as well as their bolometric correction. In Fig. 12 we show the predicted AGN LFs in the F200W band observer frame. We assume a flux limit of 9.1 nJy, which is the same as that used by Griffin et al. (2020). For sky coverage, we mimic the JWST Advanced Deep Extragalactic Survey (JADES, Williams et al. 2018). We consider three survey areas: 46, 190, and 1900 arcmin^2, which correspond to the surveys JADES-deep, JADES-medium, and ten times JADES-medium. We show the mean LF (blue solid lines) and the total field-to-field variance when assuming a 1900 arcmin^2 survey area (blue

---

[3] https://jwst-docs.stsci.edu/jwst-near-infrared-camera/nircam-instrumentation/nircam-filters

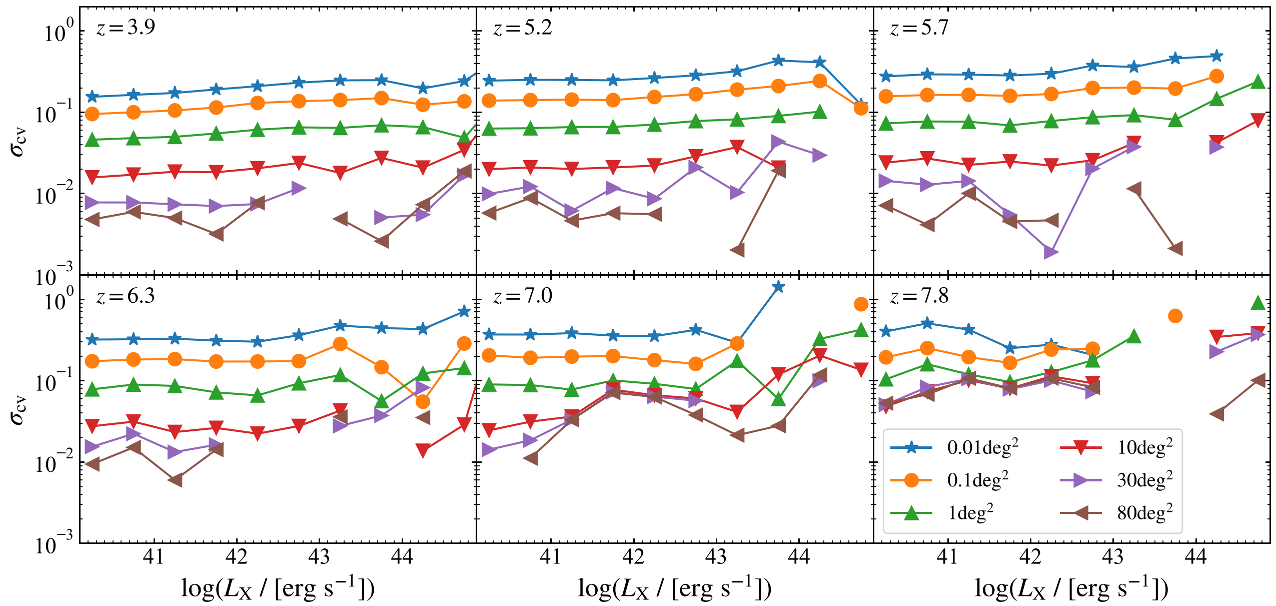

Figure 9. Cosmic variance as a function of AGN luminosity for various survey areas and at different redshifts. The comoving length of the line of sight for each survey area is shown in Table 2.

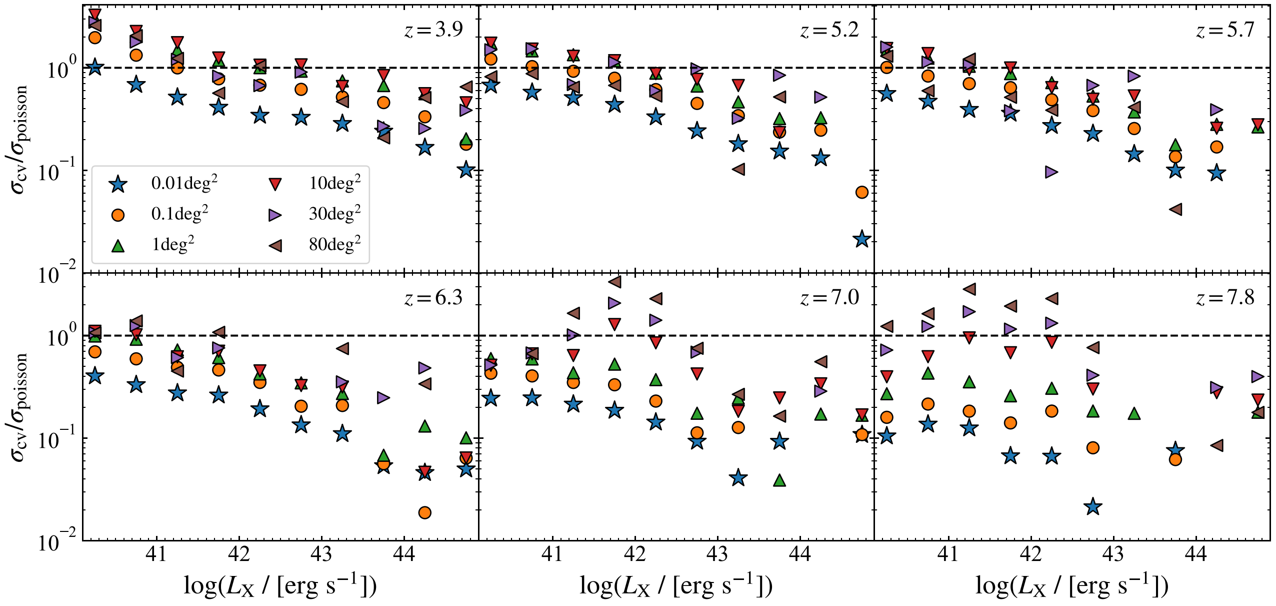

Figure 10. The ratio of the cosmic variance to Poisson variance as a function of AGN luminosity for various survey areas and at different redshifts. The comoving length of the line of sight for each survey area is shown in Table 2.

shaded regions). Invisible lower limits of the blue shaded regions in most magnitude ranges mean that no AGN can be detected given the extent of the survey area. Fig. 12 shows that even with 1900 arcmin^2 AGN cannot be detected unless the survey area has much more AGN compared to the average.

Euclid, which is scheduled for launch in 2023, will also have optical and near-IR filters at wavelengths of 0.5–2 μm. We present predictions of the AGN LF in the Euclid *H* band in Fig. 13. To derive the *H*-band magnitude, we use a set of response functions of *Euclid* filters (also including LSST filters) provided by the Euclid collaboration. Two types of surveys are planed: Euclid-deep (40 deg^2 area) and Euclid-wide (15 000 deg^2 area). Here, we use the same flux limits adopted by Griffin et al. (2020), 145 nJy for Euclid-deep and 912 nJy for Euclid-wide. The flux limits and survey areas are shown in Fig. 13. In the figure, we show the predicted variance of the AGN LF corresponding to each survey area. For Euclid-deep, we directly calculate the variance extracting regions from our Uchuu–ν^2GC volume. For Euclid-wide, we extrapolate the variance from the results up to 80 deg^2. This figure clearly shows that while Euclid-deep constrains the faint end ($M_{1450} \gtrsim -23$) of the LF, Euclid-wide can also determine the bright end ($M_{1450} \lesssim -23$).

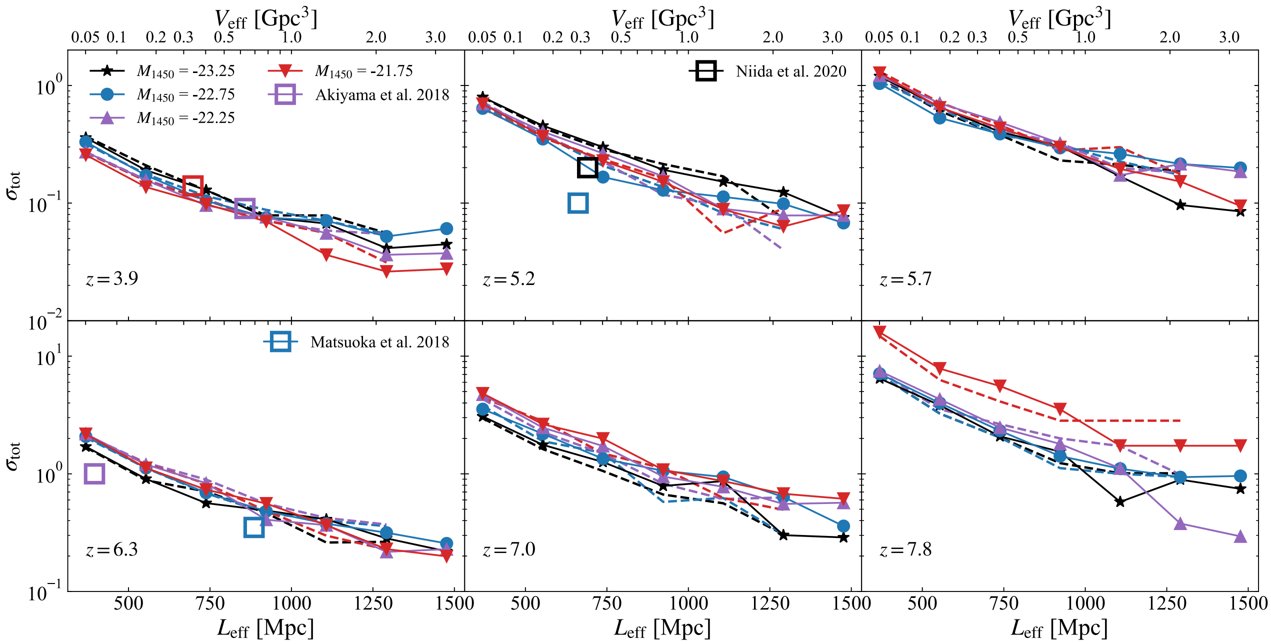

Figure 11. The total field-to-field variance as a function of effective box size $L_{\rm eff}$, corresponding to an effective survey volume $V_{\rm eff}$, for AGN samples in four luminosity ranges, M_{1450} = [–23.5, –23.0] (black), [–23.0, –22.5] (blue), [–22.5, –22.0] (purple), and [–22.0, –21.5] (red), at different redshifts. Solid lines depict the results of cubic geometries, while dashed lines depict those of cuboid geometries with depth Δz = 1. The two types of geometry have the same survey volume. The horizontal axis on the top depicts the corresponding effective survey volume. We note that the y-axes of the top and bottom panels differ in range. Open squares show the observational results from Akiyama et al. (2018), Niida et al. (2020), and Matsuoka et al. (2018). The colours indicate the range of magnitudes corresponding to the model results.

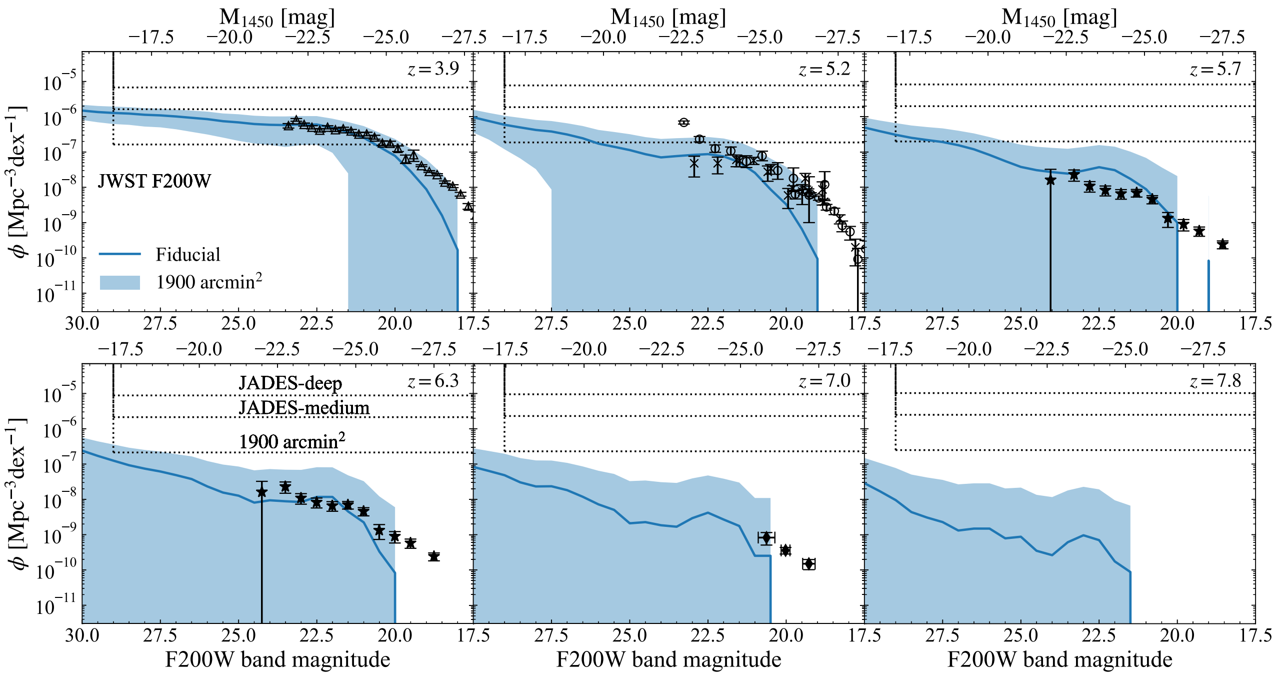

Figure 12. Predicted AGN LFs using the JWST NIRCam F200W band from z = 3.9 to z = 7.8. Blue solid lines show the result for our Uchuu–ν^2GC model with obscuration. Blue shaded regions show the total field-to-field variance of the LF when assuming a 1900 arcmin^2 survey area, ten times as large as that of the JADES-medium survey. Black data points with error bars are the same observational results as those shown in Fig. 4, but converted to apparent magnitude. The horizontal dotted lines depict the number density limit derived from the survey areas of JADES-deep (46 arcmin^2), JADES-medium (190 arcmin^2), and ten times JADES-medium (1900 arcmin^2), from top to bottom. The vertical dotted lines depict the magnitude limit derived from the flux limit adopted in this work (9.1 nJy). Objects above the horizontal line and to the right of the vertical line are detectable. The top horizontal axis shows the rest-frame UV absolute magnitude corresponding to the lower axis apparent magnitude.

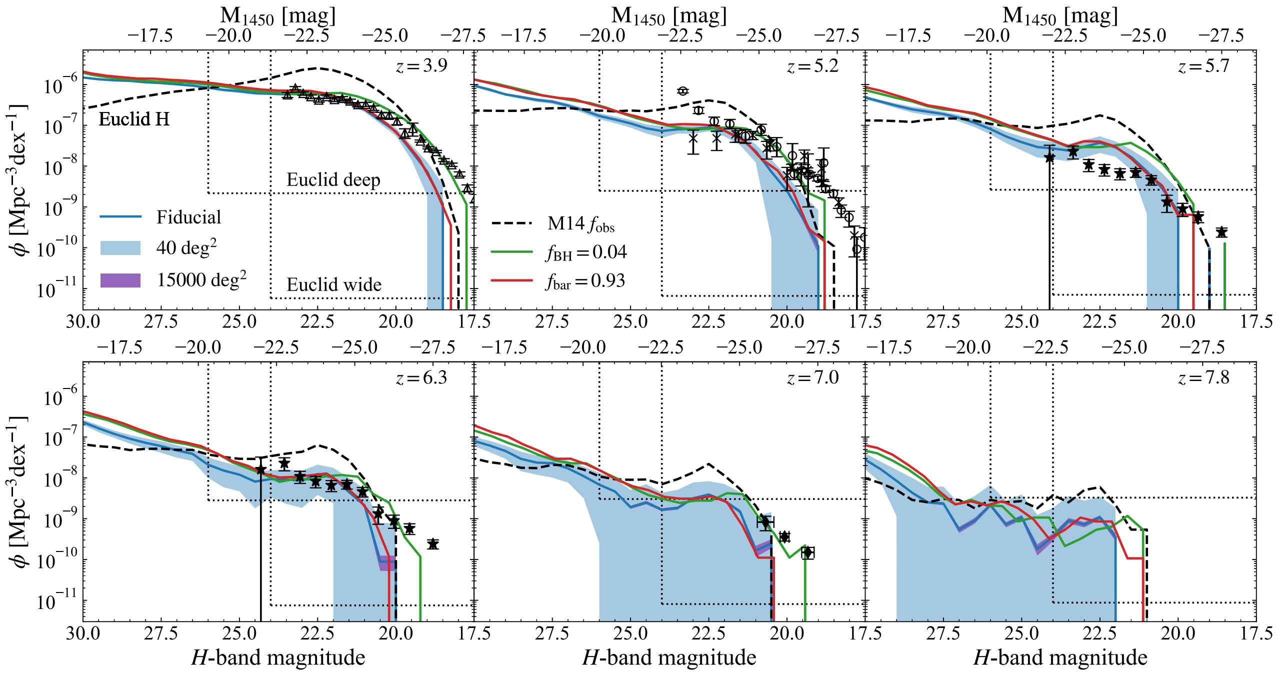

Figure 13. Same as for Fig. 12, but for both Euclid H-band surveys. Dark and light grey shaded regions show the total field-to-field variance of the LF when assuming the Euclid deep (40 deg^2) and wide (15 000 deg^2) survey area, although the latter region is almost invisible due to the small variance. The variance for 15 000 deg^2 is estimated by extrapolating from those up to 80 deg^2. For comparison, our model variants with the models $f_{\rm BH} = 0.04$ and $f_{\rm bar} = 0.93$ are also plotted (see also Fig. 4). Since the field variances of the two models are similar to that of the fiducial model, we omit them. In addition, black dashed lines show the result of the model with the observable fraction of Merloni et al. (2014). Dotted lines correspond to the magnitude limit and survey area of Euclid deep (145 nJy, 40 deg^2) and Euclid wide (912 nJy, 15 000 deg^2).

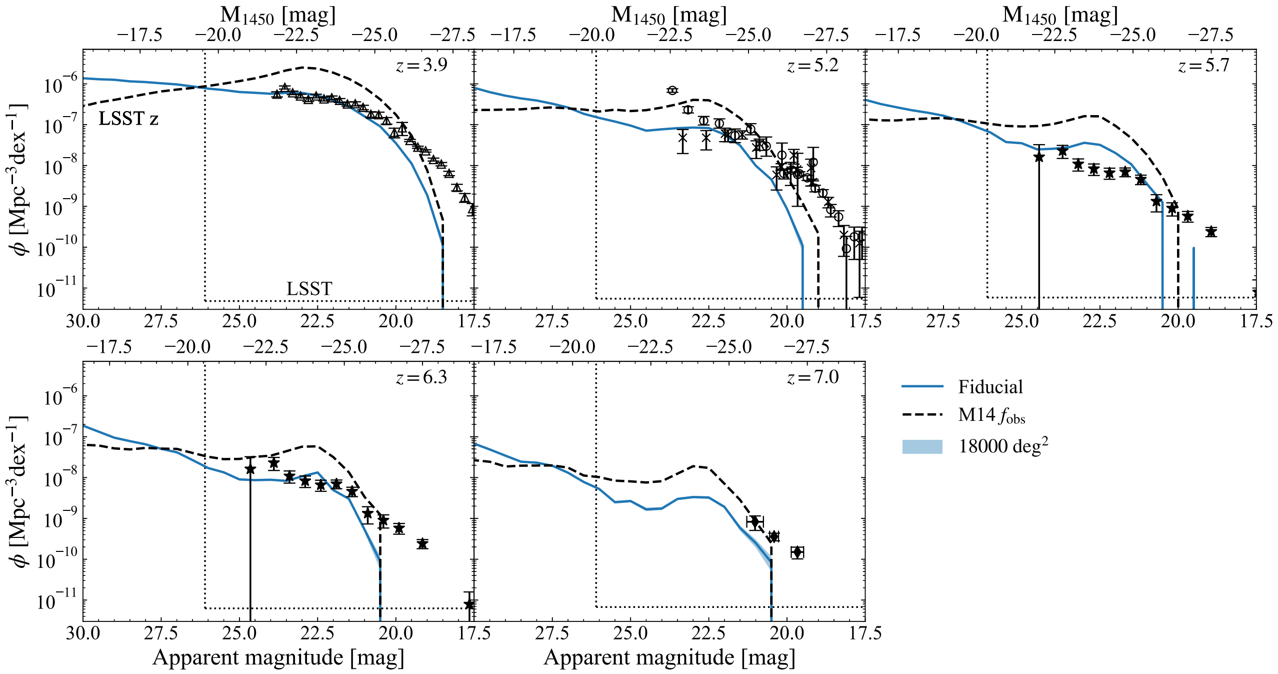

Figure 14. Same as for Fig. 12, but in the LSST z band. Blue shaded regions show the total field-to-field variance of the LF when assuming the LSST survey area (18 000 deg^2), although the region is almost invisible due to the small variance. The variance for 18 000 deg^2 is estimated by extrapolating from those up to 40 deg^2. The dotted lines correspond to the magnitude limit and survey area of the LSST survey (26.1 mag in the z band, 18 000 deg^2).

Furthermore, we study the possibility to distinguish different AGN formation models using the Euclid surveys. In Fig. 13, we also show the results of two model variants, one with $f_{\rm BH} = 0.04$ and one with $f_{\rm bar} = 0.93$; these are the same models presented in Fig. 4. While the amount of variance at the bright end can be different between the two models, the faint end variances are similar. Therefore, the parameters related to SMBH growth and AGN activity in our model do not significantly affect the variance of the AGN LF at the faint end. However, we do find a slightly larger normalization (∼0.3 dex larger) between the two model variants at the faint end than those for the fiducial model. The model with $f_{\rm BH} = 0.04$ partly reproduces the bright end of the AGN LF at $z \geq 4$ (see also Fig. 4). At $z = 6.3$, Euclid-deep may be able to constrain the AGN formation model by clarifying the faint end of the AGN LF at $\mathrm{M}_{1450} \sim -21$.

In Fig. 13, we also plot the LFs with the observable fraction of Merloni et al. (2014):

$$f_{\rm obs} = 1 - 0.56 - \frac{1}{\pi} \arctan\left(\frac{43.89 - \log L_{\rm X}}{0.46}\right), \qquad (11)$$

where $L_{\rm X}$ is the intrinsic X-ray luminosity in units of erg s^{-1}. Since the observable fraction of Merloni et al. (2014) is higher at the bright end and lower at the faint end than that of Shirakata et al. (2019), the LFs with Merloni et al. (2014) (black dashed lines) are larger than our fiducial model at the bright end, and the trend reverses at magnitudes $-20 \lesssim \mathrm{M}_{1450} \lesssim -19$. Fig. 13 shows that the faint end of the LF is sensitive to the observable fraction, which can be constrained by the new surveys with Euclid.

The LSST camera on the Vera C. Rubin Observatory[4] will discover a number of high-redshift quasars while exploring 18 000 deg^2 of the sky. In Fig. 14, we present predictions for the AGN LF in the LSST z band. We assume that the magnitude limit in the z band is 26.1, and adopt the proposed JWST area of 18 000 deg^2. As is clearly seen in this figure, the extremely large survey area and similar depth to the Euclid-deep survey will discover a large number of quasars up to $z \sim 7$. LSST will clarify the shape of the AGN LF at rest-frame UV magnitudes of $\lesssim -20.5$ at $z \sim 6 - 7$. For quasars at $z > 7$, observations with the LSST z and y bands are affected by the absorption of the inter-galactic medium. Thus, to detect such high-redshift quasars, observations with near-IR filters on JWST and *Euclid* are effective ways. In Fig. 14, we also plot the LFs with the observable fraction of Merloni et al. (2014). Like Fig. 13, Fig. 14 shows that the LF is sensitive to the observable fraction, which can be constrained by the new surveys with LSST, especially, at $z \sim 7$.

4 DISCUSSION AND SUMMARY

We have investigated the cosmic and total field-to-field variance for future galaxy and AGN surveys. To do this, we used our semi-analytic galaxy and AGN formation model, ν^2GC, with a state-of-the-art cosmological N-body simulation, the Uchuu simulation. First, we have shown that Uchuu–ν^2GC reproduces some basic population statistics of galaxies and AGN, such as the galaxy K-band LF up to $z = 3$, the cosmic SFR density, and the AGN X-ray and UV LFs over a wide redshift range. To reproduce the latter observations, we have introduced a gas accretion time-scale onto SMBHs in our model that depends on the SMBH mass and accreted gas mass.

Using this galaxy formation model, we have quantified the cosmic and total field-to-field variance for various survey configurations. We have shown that the cosmic variance of AGN does not significantly depend on their luminosities. This is because the typical DM halo mass in which AGN reside does not significantly depend on luminosity. In other words, this reflects the fact that the two-point correlation function of AGN is mostly luminosity independent in our model. Considering the field variance of the LFs of AGN, and in particular quasars (optically bright AGN), Poisson variance dominates the total variance.

We have forecast the apparent magnitude AGN LF and angular number density, or AGN number counts, in infrared bands that will be measured from surveys using JWST, *Euclid*, and LSST, taking into account the flux limit and the areas for individual surveys. From our results, the Euclid deep survey will be able to constrain the faint end of the AGN LF at $z \gtrsim 6$, even including field variance. Specifically, the Euclid deep survey can clarify the LF at the rest-frame absolute UV magnitude $\mathrm{M}_{1450} \sim -20$ at $z = 6.3$. Alternatively, the Euclid wide survey will shed light on the shape of the bright end of the AGN LF. LSST will further constrain the AGN LF by its unprecedented survey area and depth. We have also shown that the faint end of the LF is sensitive to the observable fraction, implying that the faint end can be constrained to the AGN obscuration models. Finally, we predict that JWST surveys will have a difficulty constraining the AGN LF due to their small survey areas.

While we have focused on the AGN LF in this work, understanding the relations between AGN and their host galaxies is another aspect that can be achieved by our co-evolution model of galaxy and SMBHs. Using cosmological hydrodyamical simulations, mass, SFR, and structural properties of the host galaxy have been investigated (e.g. Marshall et al. 2020; Habouzit et al. 2021). These studies, however, suffer from limited AGN numbers due to their relatively small simulation volumes. We plan to examine the properties of AGN host galaxies in more detail in a future paper.

In calculating the cosmic variance in this paper, we have used the cuboidal and cubic subvolumes in a single snapshot in this paper. In other words, we have not paid attention to the redshift dependence of the AGN LF in the analysis. This procedure can be valid if the clustering and LF evolve weakly over the $\Delta z = 1$ used. As shown in Figs 3 and 4, there is some redshift evolution in the AGN LF over the redshift range. The effect of the redshfit evolution can be taken into account by constructing observational light cones. We defer this issue to future studies.

Although we have predicted the AGN LFs for surveys with JWST, *Euclid*, and LSST (Figs 12, 13, and 14), it is often difficult to distinguish between AGN and galaxies using only one broad-band filter. Deep imaging performed by JWST can resolve the morphology of galaxies, and AGN can be identified as point sources. Effective methods to classify these two populations are therefore needed to further derive accurate AGN LFs. We will address this in future studies.

ACKNOWLEDGEMENTS

We are grateful to the anonymous referee for providing constructive comments. We thank Y. Matsuoka and ν^2GC collaboration members for useful comments and discussion. This research was supported by MEXT as 'Programme for Promoting Researches on the Supercomputer Fugaku' (JPMXP1020200109 and JPMXP1020230406) and JICFuS. This study has been funded by MEXT/JSPS KAKENHI Grant Number 23K03460, 21H05449, 20K22360, 20H01950, 18H05437, JP17H04828, JP19KK0344, and JP21H01122. Parts of this research were conducted by the Australian Research Council Centre of Excellence for All Sky Astrophysics in 3 Dimensions (ASTRO 3D), through project number CE170100013. TI has been

---

[4] https://www.lsst.org/

supported by IAAR Research Support Programme, Chiba University, Japan. SAC acknowledges funding from CONICET (PIP-2876), *Agencia Nacional de Promoción de la Investigación, el Desarrollo Tecnológico y la Innovación* (Agencia I+D + i, PICT-2018-3743), and *Universidad Nacional de La Plata* (G11-150), Argentina. RM is supported by JSPS KAKENHI Grant Number 20K14515. RM also thanks the Ministry of Science and Technology (MOST) for support through grant number MOST 108-2112-M001-007-MY3, the Academia Sinica for Investigator Award AS-IA-109-M02.

We thank Instituto de Astrofísica de Andalucía (IAA-CSIC), Centro de Supercomputación de Galicia (CESGA) and the Spanish academic and research network (RedIRIS) in Spain for hosting the Uchuu products in the Skies & Universes site (http://skiesanduniverses.org/) for cosmological simulations. The Uchuu simulations were carried out on Aterui II supercomputer at Center for Computational Astrophysics, CfCA, of National Astronomical Observatory of Japan, and the K computer at the RIKEN Advanced Institute for Computational Science. The numerical analysis was partially carried out on XC40 at the Yukawa Institute Computer Facility in Kyoto University. The Uchuu effort has made use of the skun@IAA_RedIRIS and skun6@IAA computer facilities managed by the IAA-CSIC in Spain. This equipment was funded by the Spanish MICINN EU-FEDER infrastructure grant number EQC2018-004366-P. The skun@IAA_RedIRIS server was funded by the MICINN grant number AYA2014-60641-C2-1-P. FP, AK, and JR thank the support of the Spanish Ministry of Science and Innovation funding grant number PGC2018-101931-B-I00. FP and EJ want to thank a French-Spanish international collaboration grant from CNRS and CSIC.

5 DATA AVAILABILITY

The Uchuu DR1 products and the Uchuu–ν^2GC galaxy data, a part of the Uchuu DR2 products, underlying this article are publicly available on the Skies & Universes website at http://www.skiesanduniverses.org/Simulations/Uchuu/ and https://www.skiesanduniverses.org/Simulations/Uchuu/GalaxyCatalogues/ along with the necessary documentation.

REFERENCES

Aird J., Coil A. L., Georgakakis A., Nandra K., Barro G., Pérez-González P. G., 2015, MNRAS, 451, 1892
Akiyama M., et al., 2018, PASJ, 70, 34
Amarantidis S., et al., 2019, MNRAS, 485, 2694
Atek H., Richard J., Kneib J.-P., Schaerer D., 2018, MNRAS, 479, 5184
Behroozi P. S., Wechsler R. H., Wu H.-Y., 2013a, ApJ, 762, L109
Behroozi P. S., Wechsler R. H., Wu H.-Y., Busha M. T., Klypin A. A., Primack J. R., 2013b, ApJ, 763, L18
Behroozi P. S., Wechsler R. H., Conroy C., 2013c, ApJ, 770, L57
Bhowmick A. K., Somerville R. S., Di Matteo T., Wilkins S., Feng Y., Tenneti A., 2020, MNRAS, 496, 754
Bongiorno A., et al., 2007, A&A, 472, 443
Bouwens R. J., et al., 2015, ApJ, 803, L34
Brusa M., et al., 2010, ApJ, 716, L348
Caputi K. I., McLure R. J., Dunlop J. S., Cirasuolo M., Schael A. M., 2006, MNRAS, 366, 609
Cirasuolo M., McLure R. J., Dunlop J. S., Almaini O., Foucaud S., Simpson C., 2010, MNRAS, 401, 1166
Civano F., et al., 2011, ApJ, 741, L91
Croom S. M., et al., 2005, MNRAS, 356, 415
Croom S. M., et al., 2009, MNRAS, 399, 1755
Driver S. P., et al., 2012, MNRAS, 427, 3244
Driver S. P., et al., 2018, MNRAS, 475, 2891
Duras F., et al., 2020, A&A, 636, 73
Enoki M., Ishiyama T., Kobayashi M. A. R., Nagashima M., 2014, ApJ, 794, L69
Fanidakis N., et al., 2012, MNRAS, 419, 2797
Feng Y., Di-Matteo T., Croft R. A., Bird S., Battaglia N., Wilkins S., 2016, MNRAS, 455, 2778
Fiore F., et al., 2012, A&A, 537, 16
Fontanot F., Cristiani S., Monaco P., Nonino M., Vanzella E., Brandt W. N., Grazian A., Mao J., 2007, A&A, 461, 39
Gardner J. P., et al., 2006, Space Sci. Rev., 123, 485
Giallongo E., et al., 2019, ApJ, 884, L19
Grazian A., et al., 2020, ApJ, 897, L94
Griffin A. J., Lacey C. G., Gonzalez-Perez V., Lagos C. d. P., Baugh C. M., Fanidakis N., 2019, MNRAS, 487, 198
Griffin A. J., Lacey C. G., Gonzalez-Perez V., Lagos C. d. P., Baugh C. M., Fanidakis N., 2020, MNRAS, 492, 2535
Habouzit M., Volonteri M., Somerville R. S., Dubois Y., Peirani S., Pichon C., Devriendt J., 2019, MNRAS, 489, 1206
Habouzit M., et al., 2021, MNRAS, 503, 1940
He W., et al., 2018, PASJ, 70, 33
Henriques B., Maraston C., Monaco P., Fontanot F., Menci N., De Lucia G., Tonini C., 2011, MNRAS, 415, 3571
Hirschmann M., Somerville R. S., Naab T., Burkert A., 2012, MNRAS, 426, 237
Hopkins A. M., 2004, ApJ, 615, L209
Hopkins P. F., Richards G. T., Hernquist L., 2007, ApJ, 654, L731
Hopkins P. F., Cox T. J., Younger J. D., Hernquist L., 2009, ApJ, 691, L1168
Ishigaki M., Kawamata R., Ouchi M., Oguri M., Shimasaku K., Ono Y., 2018, ApJ, 854, L73
Ishiyama T., Fukushige T., Makino J., 2009, PASJ, 61, 1319
Ishiyama T., Nitadori K., Makino J., 2012, preprint (arXiv:1211.4406)
Ishiyama T., Enoki M., Kobayashi M. A. R., Makiya R., Nagashima M., Oogi T., 2015, PASJ, 67, 61
Ishiyama T., et al., 2021, MNRAS, 506, 4210
Kawaguchi T., 2003, ApJ, 593, L69
Kawaguchi T., Shimura T., Mineshige S., 2001, ApJ, 546, L966
Krolewski A. G., Eisenstein D. J., 2015, ApJ, 803, L4
LSST Science Collaboration, 2009, preprint (arXiv:0912.0201)
Lacey C. G., et al., 2016, MNRAS, 462, 3854
Lagos C. d. P., et al., 2019, MNRAS, 489, 4196
Laureijs R., et al., 2011, preprint (arXiv:1110.3193)
Livermore R. C., Finkelstein S. L., Lotz J. M., 2017, ApJ, 835, L113
Makiya R., et al., 2016, PASJ, 68, 25
Marconi A., Risaliti G., Gilli R., Hunt L. K., Maiolino R., Salvati M., 2004, MNRAS, 351, 169
Marshall M. A., Ni Y., Di Matteo T., Wyithe J. S. B., Wilkins S., Croft R. A. C., Kuusisto J. K., 2020, MNRAS, 499, 3819
Marshall M. A., Wyithe J. S. B., Windhorst R. A., Matteo T. D., Ni Y., Wilkins S., Croft R. A. C., Mechtley M., 2021, MNRAS, 506, 1209
Matsuoka Y., et al., 2018, ApJ, 869, L150
McConnell N. J., Ma C.-P., 2013, ApJ, 764, L184
Merloni A., et al., 2014, MNRAS, 437, 3550
Mineshige S., Kawaguchi T., Takeuchi M., Hayashida K., 2000, PASJ, 52, 499
Moster B. P., Somerville R. S., Newman J. A., Rix H.-W., 2011, ApJ, 731, L113
Myers A. D., Brunner R. J., Nichol R. C., Richards G. T., Schneider D. P., Bahcall N. A., 2007, ApJ, 658, L85
Nagashima M., Yahagi H., Enoki M., Yoshii Y., Gouda N., 2005, ApJ, 634, L26
Ni Y., Di Matteo T., Feng Y., 2021, MNRAS, 509, 3043
Ni Y., Di Matteo T., Gilli R., Croft R. A. C., Feng Y., Norman C., 2020b, MNRAS, 495, 2135
Niida M., et al., 2020, ApJ, 904, L89
Ogura K., et al., 2020, ApJ, 895, L9
Ohsuga K., Mori M., Nakamoto T., Mineshige S., 2005, ApJ, 628, L368
Oogi T., Enoki M., Ishiyama T., Kobayashi M. A. R., Makiya R., Nagashima M., 2016, MNRAS, 456, 30

Oogi T., Enoki M., Ishiyama T., Kobayashi M. A. R., Makiya R., Nagashima M., Okamoto T., Shirakata H., 2017, MNRAS, 471, 21
Oogi T., Shirakata H., Nagashima M., Nishimichi T., Kawaguchi T., Okamoto T., Ishiyama T., Enoki M., 2020, MNRAS, 497, 1
Padmanabhan N., White M., Norberg P., Porciani C., 2009, MNRAS, 397, 1862
Piana O., Dayal P., Volonteri M., Choudhury T. R., 2021, MNRAS, 500, 2146
Planck Collaboration, 2020, A&A, 641, 6
Ricarte A., Natarajan P., 2018, MNRAS, 481, 3278
Richards G. T., et al., 2005, MNRAS, 360, 839
Ross N. P., et al., 2009, ApJ, 697, L1634
Saracco P., et al., 2006, MNRAS, 367, 349
Shen Y., et al., 2007, AJ, 133, 2222
Shirakata H., et al., 2016, MNRAS, 461, 4389
Shirakata H., et al., 2019, MNRAS, 482, 4846
Siana B., et al., 2008, ApJ, 675, L49
Somerville R. S., Davé R., 2015, ARA&A, 53, 51
Somerville R. S., Lee K., Ferguson H. C., Gardner J. P., Moustakas L. A., Giavalisco M., 2004, ApJ, 600, L171
Somerville R. S., Gilmore R. C., Primack J. R., Domínguez A., 2012, MNRAS, 423, 1992
Trenti M., Stiavelli M., 2008, ApJ, 676, L767
Ucci G., et al., 2021, MNRAS, 506, 202
Ueda Y., Akiyama M., Hasinger G., Miyaji T., Watson M. G., 2014, ApJ, 786, L104
Wang F., et al., 2019, ApJ, 884, L30
Waters D., Di Matteo T., Feng Y., Wilkins S. M., Croft R. A. C., 2016, MNRAS, 463, 3520
White M., et al., 2012, MNRAS, 424, 933
Williams C. C., et al., 2018, ApJS, 236, 33
Willott C. J., et al., 2010, AJ, 139, 906
Yue B., et al., 2018, ApJ, 868, L115

APPENDIX A: EXPECTED NUMBER COUNTS

In Fig. A1, we show the expected angular number density of bright AGN for these three models. We predict that 120–240 (16–80) AGN – depending on the model – with rest-frame UV absolute magnitude brighter than −20 (−20.5) will be observed at $z = 6.3$ (7) in the Euclid H-band deep survey. For the Euclid wide survey, we predict that 15 000–45 000 (3000–15 000) AGN with UV magnitude brighter than −22 (−22.5) will be detectable at $z = 6.3$ (7).

In Fig. A2, we also show the expected angular number density of bright AGN for these three models in the case of the LSST. We predict that 54 000–72 000 (10 800–18 000) AGN – depending on the model – with rest-frame UV absolute magnitude brighter than −20.5 (−21.0) will be observed at $z = 6.3$ (7) in the LSST survey.

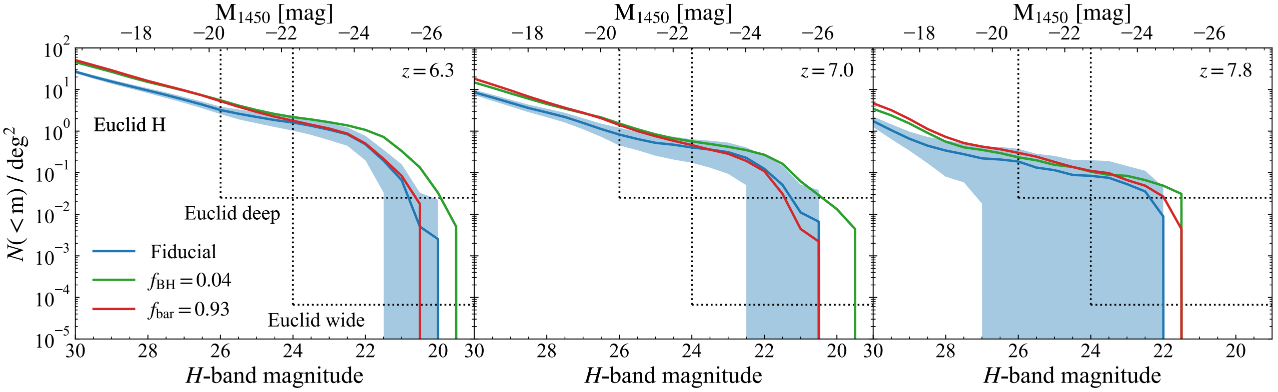

Figure A1. Expected number of AGN brighter than a given apparent H-band magnitude per square degree, showing the fiducial galaxy model (blue), model with $f_{\rm BH} = 0.04$ (green), and model with $f_{\rm bar} = 0.93$ (red). Shaded regions show the total field-to-field variance of the fiducial model when assuming a 40 deg^2 survey area, corresponding to the Euclid deep survey. Only the variance for the fiducial models is shown in order to make the figure easy to see. The amount of variances for the other two models are similar to the fiducial model. Dotted lines correspond to the magnitude limit and survey area of Euclid deep (145 nJy, 40 deg^2) and Euclid wide (912 nJy, 15 000 deg^2).

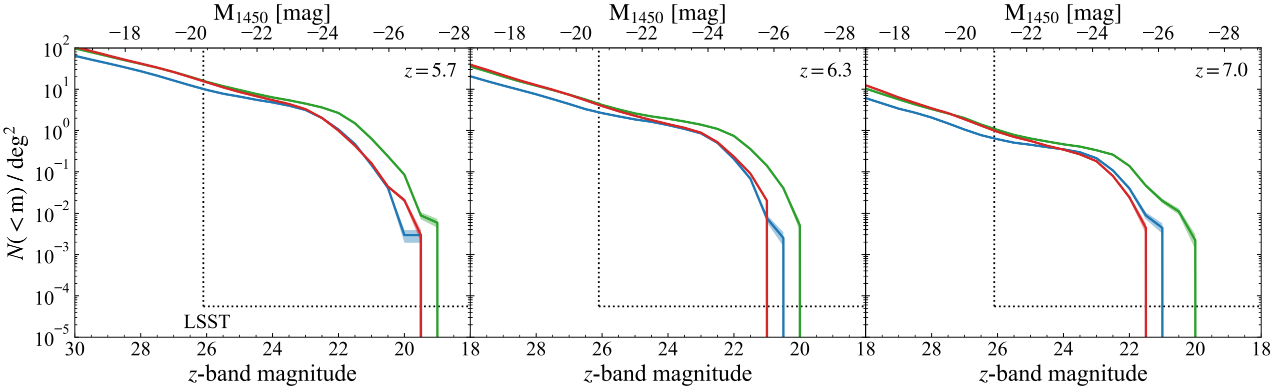

Figure A2. Same as for Fig. A1, but in the LSST z band. Shaded regions show the total field-to-field variance when assuming a 18 000 deg^2 survey area, corresponding to the LSST survey. Dotted lines correspond to the magnitude limit and survey area of the LSST survey (26.1 mag in the z band, 18 000 deg^2).

APPENDIX B: DATA BASE RELEASE

All Uchuu–ν^2GC data used for this paper are publicly available in our Skies & Universes website. While we refer to Section 2.2 (and references therein) for a description of the model, we list in Table B1 a subset of the galaxy properties included in the Uchuu–ν^2GC public catalogue. We further encourage the reader to visit the data base for the additional documentation provided there, as the list of galaxy properties is not limited to what is shown in Table B1.

Table B1. Set of galaxy properties in the Uchuu–ν^2GC catalogue. Note that x, y, z, v_x, v_y, v_z, HaloMass, and Vmax for orphan galaxies have been set to those for the host halo in Uchuu–ν^2GC. Also note that additional properties to those listed here have been included in the publicly available Uchuu–ν^2GC data; refer to the data base website for more information.

Data base name	Unit	Description
HostHaloID	n/a	Pointer to DM halo in which galaxy resides; identical to id in the ROCKSTAR halo catalogue, not applicable for orphan galaxies
MainHaloID	n/a	Pointer to DM halo in which galaxy orbits
GalaxyType	n/a	0 = central galaxy 1 = satellite galaxy 2 = orphan galaxy
X	comoving h^{-1} Mpc	x-position of galaxy
Y	comoving h^{-1} Mpc	y-position of galaxy
Z	comoving h^{-1} Mpc	z-position of galaxy
Vx	peculiar km s^{-1}	v_x-velocity of galaxy
Vy	peculiar km s^{-1}	v_y-velocity of galaxy
Vz	peculiar km s^{-1}	v_z-velocity of galaxy
MstarBulge	h^{-1} M$_\odot$	Stellar mass of bulge component of galaxy
MstarDisc	h^{-1} M$_\odot$	Stellar mass of disc component of galaxy
McoldBulge	h^{-1} M$_\odot$	Cold gas mass of bulge component of galaxy
McoldDisc	h^{-1} M$_\odot$	Cold gas mass of disc component of galaxy
Mhot	h^{-1} M$_\odot$	Total hot gas mass in galaxy
Mbh	h^{-1} M$_\odot$	Mass of central black hole
SFR	h^{-1} M$_\odot$ Gyr^{-1}	SFR
MeanAgeStars	Gyr	Rest frame V-band luminosity weighted stellar age
HaloMass	h^{-1} M$_\odot$	$M_{\rm vir}$ of galaxy's DM halo
Vmax	km s^{-1}	Peak circular rotation velocity of galaxy's DM halo
Concentration	n/a	Concentration of galaxy's DM halo, −1 for orphan galaxies
SpinParameter	n/a	Spin parameter λ of galaxy's DM halo, −1 for orphan galaxies
ZstarBulge	n/a	Mass-weighted mean stellar metallicity of bulge, −99 for no bulge stars
ZstarDisc	n/a	Mass-weighted mean stellar metallicity of disc, −99 for no disc stars
MZgasDisc	M$_\odot$	Mass of metals in gas component of disc
LumAgnBol	erg s^{-1}	AGN bolometric luminosity
LumAgnXray	erg s^{-1}	AGN hard X-ray (2–10 keV) luminosity
MagAgnUV	n/a	AGN UV (1450 Å) magnitude, 128 for no AGN activity
Rest-frame magnitudes:		
MagStar(d)_SDSSu	n/a	Dust uncorrected (corrected) absolute magnitude in SDSS u band
MagStar(d)_SDSSg	n/a	Dust uncorrected (corrected) absolute magnitude in SDSS g band
MagStar(d)_SDSSr	n/a	Dust uncorrected (corrected) absolute magnitude in SDSS r band
MagStar(d)_SDSSi	n/a	Dust uncorrected (corrected) absolute magnitude in SDSS i band
MagStar(d)_SDSSz	n/a	Dust uncorrected (corrected) absolute magnitude in SDSS z band
MagStar(d)_2MASSJ	n/a	Dust uncorrected (corrected) absolute magnitude in 2MASS J band
MagStar(d)_2MASSH	n/a	Dust uncorrected (corrected) absolute magnitude in 2MASS H band
MagStar(d)_2MASSK	n/a	Dust uncorrected (corrected) absolute magnitude in 2MASS Ks band
MagStar(d)_GALEXFUV	n/a	Dust uncorrected (corrected) absolute magnitude in *GALEX* FUV band
MagStar(d)_GALEXNUV	n/a	Dust uncorrected (corrected) absolute magnitude in *GALEX* NUV band
Observer-frame magnitudes:		
AppMagStar(d)_SDSSu	n/a	Dust uncorrected (corrected) apparent magnitude in SDSS u band
AppMagStar(d)_SDSSg	n/a	Dust uncorrected (corrected) apparent magnitude in SDSS g band
AppMagStar(d)_SDSSr	n/a	Dust uncorrected (corrected) apparent magnitude in SDSS r band
AppMagStar(d)_SDSSi	n/a	Dust uncorrected (corrected) apparent magnitude in SDSS i band
AppMagStar(d)_SDSSz	n/a	Dust uncorrected (corrected) apparent magnitude in SDSS z band
AppMagStar(d)_HSCg	n/a	Dust uncorrected (corrected) apparent magnitude in HSC g band
AppMagStar(d)_HSCr	n/a	Dust uncorrected (corrected) apparent magnitude in HSC r band
AppMagStar(d)_HSCi	n/a	Dust uncorrected (corrected) apparent magnitude in HSC i band
AppMagStar(d)_HSCz	n/a	Dust uncorrected (corrected) apparent magnitude in HSC z band
AppMagStar(d)_HSCy	n/a	Dust uncorrected (corrected) apparent magnitude in HSC y band

This paper has been typeset from a TEX/LATEX file prepared by the author.

Published by Oxford University Press on behalf of Royal Astronomical Society